Architecture of the *Xenopus* Nuclear Pore Complex Revealed by Three-Dimensional Cryo-Electron Microscopy

Christopher W. Akey and Michael Radermacher*

Department of Biophysics, Boston University School of Medicine, Boston, Massachusetts 02118-2394; and *Wadsworth Center for Laboratories and Research, New York State Department of Health, Albany, New York 12201-509

Abstract. The nuclear pore complex spans the nuclear envelope and functions as a macromolecular transporter in the ATP-dependent process of nucleocytoplasmic transport. In this report, we present three dimensional (3D) structures for both membrane-associated and detergent-extracted *Xenopus* NPCs, imaged in frozen buffers by cryo-electron microscopy. A comparison of the differing configurations present in the 3D maps suggests that the spokes may possess an intrinsic conformational flexibility. When combined with recent data from a 3D map of negatively stained NPCs (Hinshaw, J. E., B. O. Carragher, and R. A. Milligan. 1992. *Cell.* 69:1133–1141), these observations suggest a minimal domain model for the spoke–ring complex which may account for the observed plasticity of this assembly. Moreover, lumenal domains in adjacent spokes are interconnected by radial arm dimers, forming a lumenal ring that may be responsible for anchoring the NPC within the nuclear envelope pore. Importantly, the NPC transporter is visualized as a centrally tapered cylinder that spans the entire width of the NPC, in a direction normal to the nuclear envelope. The central positioning, tripartite structure, and hollow nature of the transporter suggests that it may form a macromolecular transport channel, with a globular gating domain at each end. Finally, the packing of the transporter within the spokes creates a set of eight internal channels that may be responsible, in part, for the diffusion of ions and small molecules across the nuclear envelope.

THE nuclear pore complex (NPC)[1] resides within a pore formed by the fusion of the inner and outer nuclear membranes and is tethered to the nuclear lamina. Therefore, the NPC is ideally situated to mediate the bidirectional exchange of small molecules and catalyze the active transport of proteins, cellular and viral RNPs (15, 25, 29, 48). Accumulating evidence suggests that nucleocytoplasmic transport is a singular reaction in that: (*a*) transport is bidirectional yet vectorial for a particular substrate at a given instant; (*b*) transport occurs through the center of the NPC as visualized by thin sections of Balbiani ring mRNPs transiting the NPC (61); (*c*) an unusually broad range of substrate types and sizes are transported; (*d*) substrates need not be deformed in passage (21); (*e*) the import of many karyophilic proteins is dependent on a positively charged nuclear localization signal (NLS), that is bipartite in nucleoplasmin and SWI5 (43, 56); and (*f*) import of karyophilic proteins requires at least two cytosolic factors (1, 44, 45) and involves specific binding to O-linked N-acetyl glucosamine containing nucleoporins (58).

Substrates transported by the NPC are chemically diverse and include: proteins, mRNPs, snRNPs, pre-ribosomal subunits, and tRNAs. Recent data suggests that they use a common transport machine located within the NPC, as both import and export reactions for these substrates demonstrate ATP-dependent saturation kinetics (9, 14, 30, 41, 46, 65) and manifest similar inhibition profiles (13, 14, 19, 24, 41). Interestingly, protein import and the export of nucleic acids appears to occur through common NPCs (17). In addition, the transport of proteins and mRNPs are topologically similar, as both processes use a central channel within the NPC that constrains substrates to a maximum diameter of 200–250Å during translocation (28, 61, 23, 40). The identity and structure of the macromolecular transport machine located centrally within the NPC has not been established.

The NPC is a cylindrical assembly with octagonal symmetry and a mass of ~125 Mda (18, 52). Disassembly studies (52, 62) and quantitative image analyses of en face and side-on projections have suggested that the NPC is comprised of a set of thin rings which sandwich a more massive spoke assembly (3, 52, 62). Projections of frozen-hydrated specimen have revealed pairs of radial arms that interconnect adjacent spokes and a central ringlike transporter (3), that may be capable of forming a gated transport channel for substrates (4, 8). The precise symmetry of the NPC proper may vary depending on structural changes induced

1. *Abbreviations used in this paper*: CP, cytoplasmic particles; CR/NR, cytoplasmic ring/nucleoplasmic ring; CTF, contrast transfer function; ISR, inner spoke ring; NLS, nuclear localization signal; NPC, nuclear pore complex; RA, radial arm; 3D, three dimensional.

during enucleation and sample preparation (3). The NPC may be either eightfold symmetric about an axis perpendicular to the nuclear envelope (3, 18, 28, 52) or ~822 symmetric with an approximate twofold axis relating the oppositely facing halves of the spoke–ring complex (3, 4, 42, 62). Recently, Hinshaw and co-workers (34) have completed a single particle three-dimensional (3D) reconstruction from detergent-extracted (dform) and detached *Xenopus* NPCs with ~822 symmetry. As visualized in negative stain, the minimal building block of the spoke–ring complex is composed of five domains including two domains within each of the averaged thin rings and three domains in each half-spoke. Peripheral assemblies, such as cytoplasmic particles, filaments (28, 53, 54, 55, 59, 62), and nucleoplasmic cages/baskets (28, 36, 54, 55) were not visualized in these detached specimens.

In this report, we present data from independent 3D reconstructions of *Xenopus* NPCs tethered to the nuclear lamina in the presence or absence of the nuclear envelope. The maps provide insights on issues concerning: (*a*) the minimal domain structure of the spoke–ring complex and its observed conformational flexibility; (*b*) the possible role of the NPC transporter in nucleocytoplasmic transport; (*c*) the positions of internal channels that may function as diffusion pores; and (*d*) interactions between the NPC and the encircling nuclear envelope.

Materials and Methods

Specimen Preparation and Image Processing

The maintenance of amphibians, isolation of oocytes, and preparation of frozen-hydrated nuclear envelope spreads for cryo-electron microscopy were carried out as described previously (3). Two microscopes were used in the data collection, a Philips EM400T at the Deptartment of Cell Biology, Stanford University Medical School (Stanford, CA) and an EM400 in the Structural Studies Division at the Medical Research Council Laboratory of Molecular Biology. Both microscopes were modified with objective lens current meters by Dr. C. Toyoshima (Department of Biological Sciences, Tokyo Institute of Technology, Tokyo, Japan) which were used to adjust the zero and tilted specimen pair z-heights, such that a consistent objective lens current was obtained, thereby ensuring a uniform magnification. Micrographs were scanned on a flatbed densitometer manufactured by Joyce, Loebl and Co. Ltd. (Gateshead, England), that was extensively modified at the LMB. The effective step sizes on the images were 24.6 and 26.7Å, depending on the initial magnification. 3D image processing used SECReT, a 3D reconstruction method for single particles based on a conical tilt geometry (50, 51), implemented within the SPIDER software package (26). A suite of roughly 100 SPIDER procedures and sub-procedures were written and integrated into a single automated 2D/3D program set, ALIGN_EM, based in part on a previous set of programs written by M. Radermacher (New York State Department of Health, Albany, NY) (RCDOALL). ALIGN_EM runs five deep within a batch job and provides a highly structured environment for data and document files during the analysis of large datasets. The current version has over 40 steps in a sequential menu driven format that covers 2D/3D alignments and the preparation of computed 3D maps for subsequent analysis and presentation.

Specific modifications were made in the procedures used to align tilted particles, to accommodate the low-contrast images of frozen-hydrated specimens. In particular, larger areas of 256 × 256 were windowed out around the zero and tilted particles and used only in the alignment of the untilted/tilted image pairs, to boost the signal of the cross-correlation peak. Images in 128 × 128 format were used routinely for all other calculations. In addition, all tilted particles used in the 3D reconstructions had the first minima of their contrast transfer functions (CTFs) outside the nominal resolution range. Cylindrical averages of the tilted and aligned particles were used to judge the accuracy of alignment along with the convergence of the step sizes assigned to each particle during refinement. Further improvements in the tilt centration parameters were achieved by iterative refinement of each tilted image against a projection of an unweighted 3D reconstruction, calculated from the entire dataset (Radermacher, 1992). In this approach the tilted image under refinement (with negative contrast) was removed from the trial 3D reconstruction by back projection, before a centration alignment between the original tilted image (with positive contrast) and the equivalent projection calculated from the 3D volume. Corrected xy shifts were then used to reinsert the tilted image into the 3D volume by back projection and the process continued for all images in the dataset through two complete cycles. This refinement resulted in small but significant changes in the xy shifts obtained from cross-correlational alignments of the zero/tilted image pairs.

Datasets with tilt angles of 34° (mform) and 42° (dform) were used to minimize problems from nearest neighbor overlap in the tilted specimens; however this resulted in rather large missing cones. Therefore, a real space/Fourier space method (POCs/solvent flattening; 12) was employed that uses volume constraints to iteratively extend the molecular transform into the cone of missing information. This approach was incorporated into SPIDER by M. Radermacher and carried out as follows. A weighted 3D reconstruction of the complete dataset was used to generate a 3D mask of the NPC using a combination of thresholding and low pass filtering. The mask was then applied to the 3D volume in real space and the 3D Fourier transform calculated. The resulting molecular transform in the missing cone was left untouched between cycles, but the calculated Fourier in the measured area of the molecular transform was replaced with the original molecular transform (from the unmasked object) and the resulting hybrid back Fourier transformed. This procedure was carried out for two to three cycles before defining a smaller mask and repeating the process. The final molecular volume of the mask was roughly 1.5 times the calculated molecular volume of the NPC based on STEM mass measurements (52). This cutoff was used to compensate for the unknown mass and undetermined occupancy of the cytoplasmic particles and material "trapped" within the transporter (4). Solvent flattening produced 3D maps whose peak distribution and relative intensities were unaffected in the xy plane sections; however, the modified maps demonstrated a higher contrast relative to background and a net shrinkage along the z-axis of 12–16%, resulting in height/diameter ratios that agree with side-on views (3). The series of 3D masks were used to refine half-datasets in parallel and the resulting 3D maps used to calculate phase residuals (27). Phases within the missing cone were random at the beginning of POCs refinement, but converged to give residuals similar to those in the original measured regions of the molecular transform (~100Å). Final 3D volumes were merged from the half-datasets and low pass filtered at 80Å resolution to compensate for doubling the amount of data. The POCs method worked well because the original NPCs are not appreciably flattened in the frozen-hydrated state. Moreover, an excellent fit of common features was obtained when the central sections in each map were scaled together, but regions within the scaled maps corresponding to the thin rings in the mform were 6–10% smaller in diameter than their counterparts from the dform. Multicolor surface rendering techniques were used to highlight specific regions within the 3D maps using an algorithm written by M. Radermacher to create a composite surface for display on WEB, a Motif display program written by A. Leith (New York State Department of Health, Albany, NY). Cutoffs were chosen to illustrate reproducible features and generally fell at the boundaries of steep density gradients. Unknown parameters such as the absolute occupancy of cytoplasmic particles and material caught in transit within the transporter, coupled with uncertainties arising from the loss of the lowest resolution frequencies of the CTF, prevented us from placing the surface maps on an absolute volume scale commensurate with the measured mass (52).

Results

We have used cryo-electron microscopy of frozen-hydrated specimens to visualize the architecture of the NPC in 3D. This approach minimizes perturbations that can occur during negative staining and drying of large specimens. These methods have produced both pseudosymmetric (~822) and asymmetric (C8) averages of the NPC associated with either the nuclear envelope or the nuclear lamina (3, 4, 7). We have used the Single Exposure random Conical tilt Reconstruction Technique (SECReT; 50, 51) which uses a pair of micrographs, one tilted and one untilted, to obtain the orientation angles necessary to calculate 3D maps from tilted projections. Maps of membrane-associated (mform) and detergent-

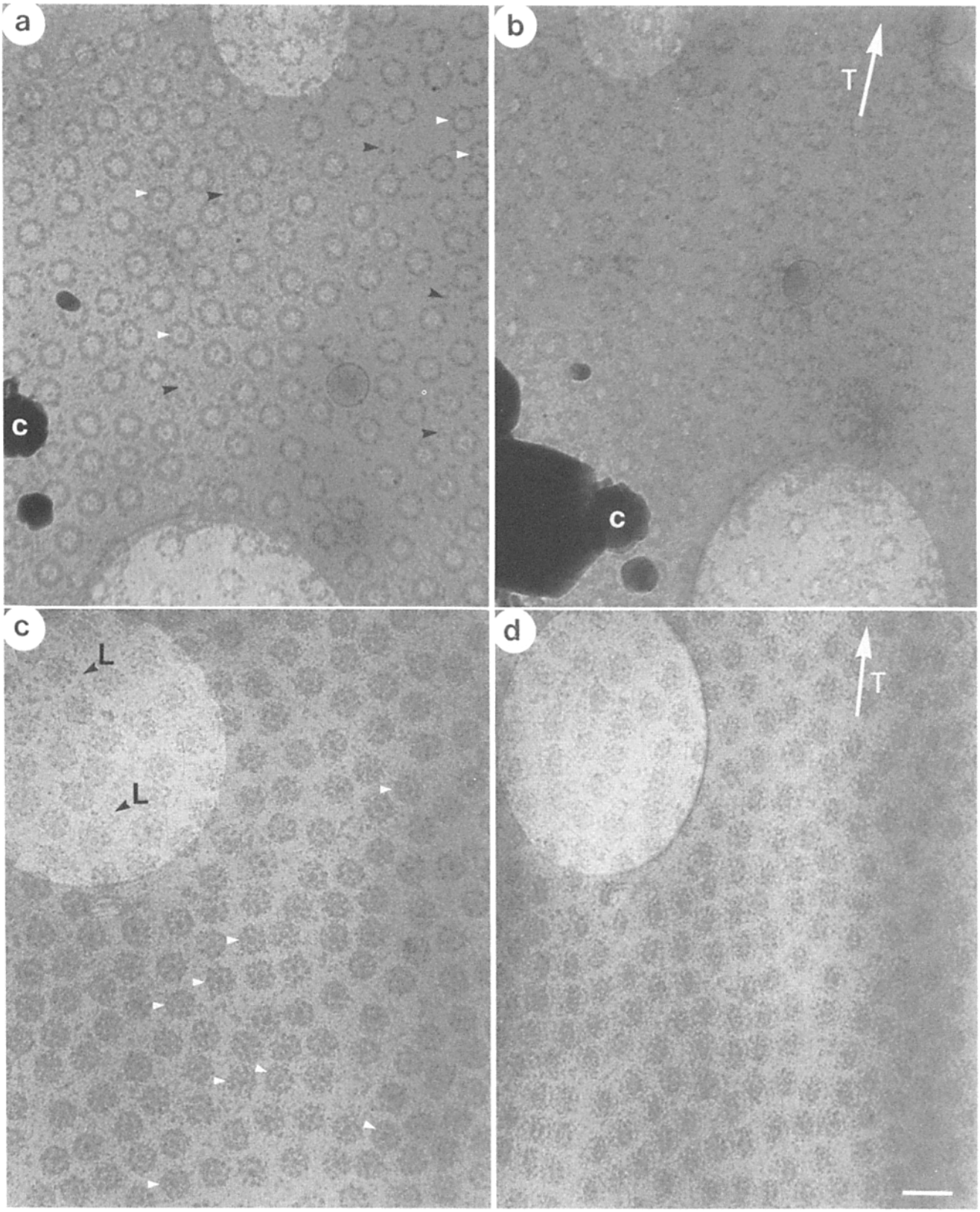

Figure 1. Representative areas of electron micrographs of zero/tilt pairs of frozen-hydrated *Xenopus* NPCs are shown. Note that the circular NPCs become elliptical in the tilted images and show evidence of the triple ring morphology. (*a* and *b*) Zero and 34° tilt images of membrane-associated NPCs. Dark areas are protein with the exception of crystalline ice particles (*c*). Large particles associated with the nuclear envelope are visible in the spaces between NPCs (*black arrowheads* in *a*). The position of the tilt axis is indicated by the white arrow in *b*. NPCs with central transporters are indicated with white arrowheads. (*c* and *d*) Zero and 42° tilt image pair recorded from a *Xenopus* macronucleus extracted with TX-100. The tilt axis position is marked by the white arrow in *d*. Ringlike NPC transporters are present with high occupancy in the zero tilt NPCs (*white arrowheads* in *c*) and the lamina is present as a fine meshwork between the NPCs (*L*). Bar, 2,000 Å.

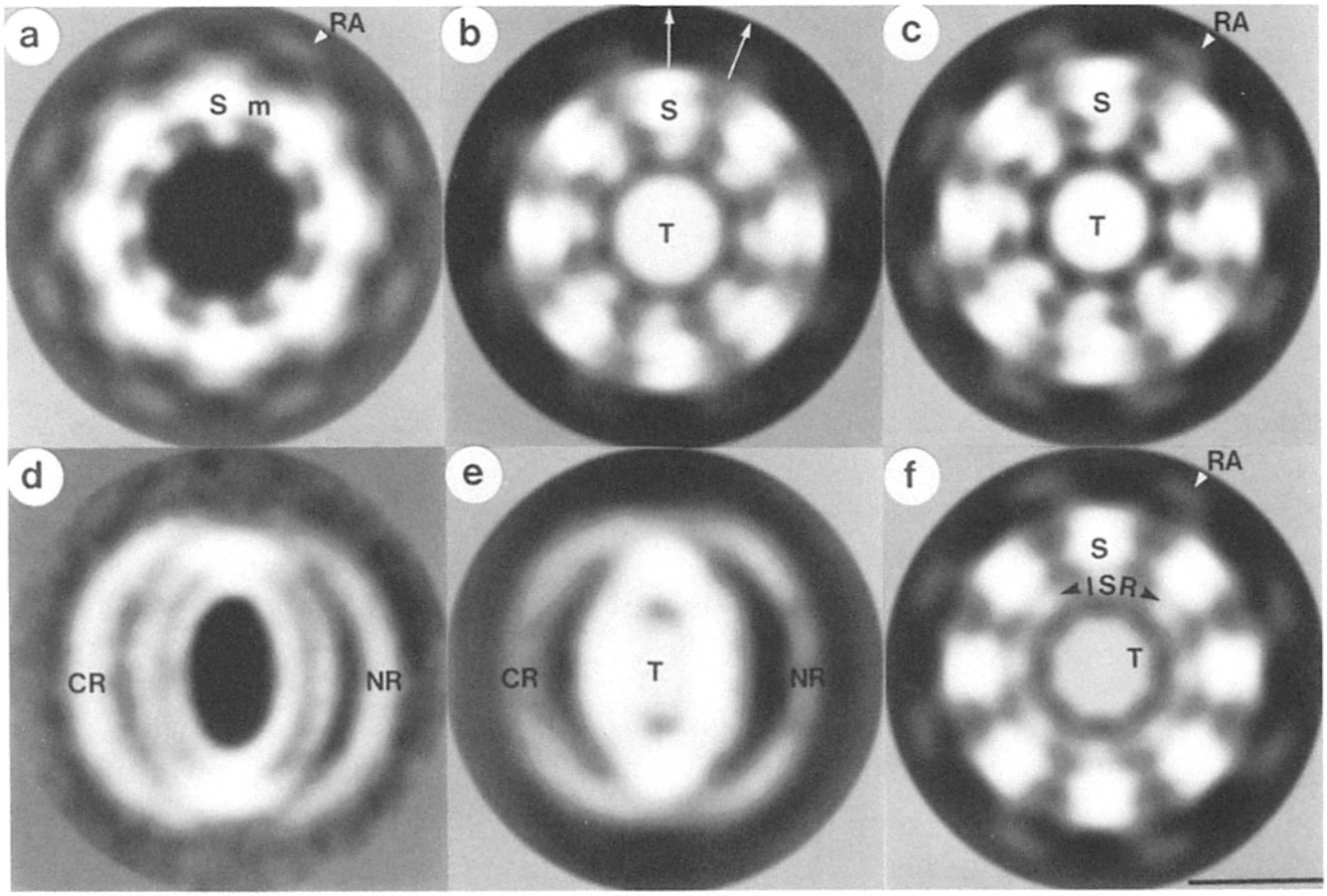

Figure 2. Projection maps of both untilted (eightfold averaged) and tilted (cylindrically averaged) frozen-hydrated NPCs; contrast is reversed with protein and strongly scattering material white. The maximum diameter of the untilted NPCs excluding the radial arms is 1,200 Å. (*a*) Map from 196 *Xenopus* membrane-associated NPCs; the spokes (*S*), radial arms (*RA*), and the membrane border (*M*) are indicated. (*b*) Map of *Xenopus* detergent-extracted form calculated from 284 NPCs. Substructure is labeled as above with the exception of the central NPC transporter (*T*), which appears in this view as an averaged plug. The positions of approximate twofold axes aligned with the spokes and radial arms are indicated by white arrows. (*c*) A map of 268 NPCs obtained from a second detergent-extracted nuclear ghost is shown. Note the similarity to the map in *b*. (*d*) A cylindrical average obtained from tilted and aligned NPCs (n = 196) associated with the nuclear envelope is shown. The ring of spokes and the membrane border are present as an elliptical doublet; the thin cytoplasmic and nucleoplasmic rings (*CR* and *NR*) are labeled. (*e*) A cylindrical average of detergent-extracted NPCs (n = 284) is shown. The NPC transporter forms a broad band of density along the horizontal axis. (*f*) Map from 284 *Necturus* NPCs associated with a detergent-extracted nucleus isolated from an animal with unhealthy oocytes. Note the weak inner spoke ring (*ISR*) formed by the slewed inner spoke domains. Density within the spokes is somewhat asymmetric. Bar, 500 Å.

extracted (dform) NPCs from *Xenopus* were obtained by this method and are described in the following sections. At this stage, the resolution is inadequate to precisely identify subunit boundaries within the molecular envelopes of the maps. However, a detailed side-by-side comparison allows a qualitative description of the minimal number of domains which comprise the framework of the spoke–ring complex. This analysis confirms the 3D map of Hinshaw and coworkers (34) and extends our understanding of the conformationally flexible spoke–ring assembly and its interactions with the central NPC transporter.

NPCs Associated with the Nuclear Envelope

Representative areas of a micrograph pair recorded at 0° and 34° from a spread *Xenopus* nuclear envelope are shown in Fig. 1, *a* and *b*. The mform NPCs used for the 3D reconstruction were circular with a distinct eightfold symmetry and demonstrated a ring of density centered at a radius of ~420–430Å that traverses the centers of individual spokes in projection (3, 4, 36, 62). The specimens are unstained; hence, protein dominates the scattering and is dark. The tilt axis (34°) is located parallel to the white arrow in Fig. 1 *b*, along the major axis of the elliptical NPCs in the tilted image. Although a few NPCs retain their ringlike central transporters (*white arrowheads* Fig. 1 *a*), the majority have lost them during specimen preparation. In addition, large particles located between the NPCs (indicated by *black arrowheads*) may correspond to either detached cytoplasmic particles observed in the 3D maps or possibly to membrane-associated ribosomes (62).

Averaged projection maps resulting from computer-based alignments of untilted and tilted (34°) NPCs are shown in Fig. 2, *a* and *d*. Contrast has been reversed relative to the micrographs; protein is now white. The averaged map calculated from the untilted NPCs is similar to maps obtained previously from *Xenopus* (3). For example, the eight spokes and

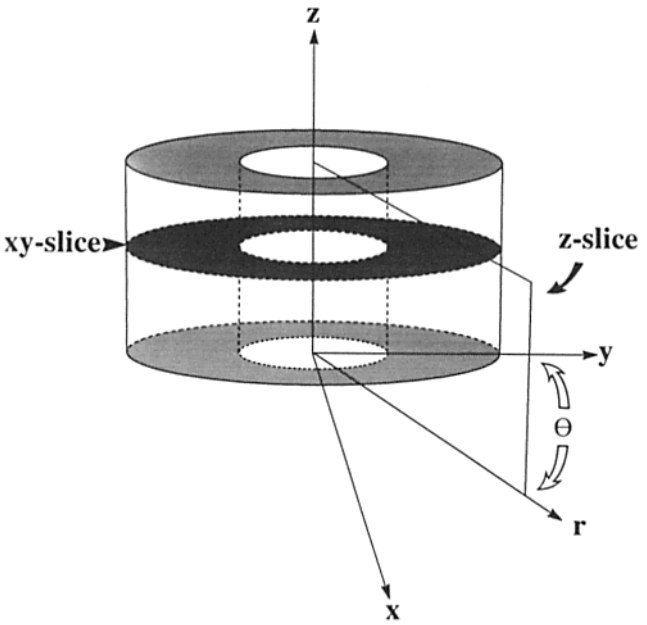

Figure 3. Diagram of a model cylinder with the x-, y- and z-axes indicated. The slices described in the text are shown including an xy slice cut perpendicular to the z-axis (the dark plane) and a z-slice which corresponds to a cross-section cut parallel to and containing the z-axis. As an example, a z slice is shown cut along an arbitrary radial axis denoted by the angle theta. The z slices described in the text were chosen as follows. The spoke z slice was chosen to bisect individual spokes along their approximate twofold axis. Radial arm z slices were obtained by rotating the plane of the cross-section by 22.5° clockwise, thereby bisecting the radial arms and the inner spoke ring.

their attachments to the radial arms are visible. In addition, the spokes are bisected by a ring of density that may arise from the border of the fused inner and outer nuclear membranes. The transporter is absent from the 2D map; instead a central cavity is present with a diameter of ~440Å (Fig. 2 *a* and see Fig. 4). A cylindrically averaged map was calculated from the tilted and aligned NPCs (Fig. 2 *d*). A cylindrical average is obtained because all possible rotational orientations, relative to the central eightfold axis, are present in the corresponding untilted NPCs. Hence, after tilting to 34° and averaging over 196 NPCs a rotationally "blurred" image is obtained without subunit details as viewed from above. Importantly, the cylindrical average provides direct evidence that the cytoplasmic and nucleoplasmic rings are present within the specimens. Moreover, the membrane border and spoke subunits appear to be split into concentric elliptical rings that "encircle" the central cavity. After the tilted NPCs were aligned to a common origin, a 3D map was calculated by back projection. The cytoplasmic and nucleoplasmic sides were then identified as follows. First, features within the map could be correlated directly with their counterparts in the 3D map of the dform. This form possesses a distinct handedness in projection that has been used previously to assign a unique viewing direction (3). Second, the cytoplasmic ring in the maps was "denser" due to the presence of the cytoplasmic particles. This observation is in agreement with previous observations (33, 52, 55, 62).

After refinement, differing views of domains within the 3D maps were obtained by taking appropriate xy slices or z slices (cross-sections) of the 3D volume. The orientation of xy slices cut perpendicular to the z-axis is shown in Fig. 3, within an idealized cylindrical volume. In Fig. 3, the z-axis would correspond to the central eightfold symmetry axis of the NPC. A set of xy-slices for the mform is shown in Fig. 4 (*a–f*), and the spacings of these slices are shown in a side view of a surface model to orient the reader (Fig. 4 *g*). The 3D map demonstrates an approximate twofold axis of symmetry within the central section (arrows *1* and *2* in Fig. 4 *d*) that is maintained within the spokes. Symmetry axis 1 is centered on each spoke while symmetry axis 2 is rotated 22.5° clockwise from axis 1 and bisects the radial arms. In total, both approximate twofold axes are repeated eight times around the cylindrical NPC. The approximate twofold symmetry of the spokes is shown by comparing xy-slices in Fig. 4, *c* and *f*, which are related by a 180° rotation about the center of the spokes. However, the thin rings are different at this resolution (80–100Å) with the cytoplasmic ring having eight paired domains (labeled *1* and *2*) and an inwards pointing aspect (see *asterisk* in Fig. 4 *b*), while the nucleoplasmic ring has eight contiguous single domains and is less intense (compare Fig. 4, *b* and *e*). Furthermore, the departure from perfect twofold symmetry is most marked at the cytoplasmic ring which is decorated with the remnants of cytoplasmic particles or collapsed filaments (see Fig. 4 *a*). The centers of the cytoplasmic particles are offset counterclockwise by ~17° from the putative spoke twofold axis (symmetry axis "1" in Fig. 4 *d*).

Inspection of the central xy slice in Fig. 4 *d* reveals three density peaks within each spoke including: the inner domain (IS), a central domain (CS), and the lumenal domain (LS). Furthermore, certain spoke domains join together to form larger concentric structures. For example, the inner spoke domains are interconnected to form an inner spoke ring (ISR) and the lumenal domains penetrate into the nuclear lumen where they are linked by radial arm dimers (RA), forming a lumenal ring. Additional features are visible in z-slices, as defined in Fig. 3, that correspond to planar cross-sections cut parallel to the z-axis along the arrows labeled *1* and *2* in Fig. 4 *d*. In Fig. 5 *a*, the z-slice bisects a spoke showing the vertical and radial density variations within oppositely facing spokes. Interestingly, the inner spoke domains make their strongest contacts to the rodlike density that contains the central domain at the upper and lower extremities, rather than at the midline. Other contributions to the vertical rod-shaped density result from the juxtaposition of the outer vertical domains (Vo) and the central domain with the nuclear envelope border. The lumenal spoke domain protrudes from the spoke surface into the lumen of the nuclear envelope. A second cross-section cut 22.5° away and bisecting the radial arms, shows portions of five domains including the ISR, the cytoplasmic and nucleoplasmic rings (CR/NR), the cytoplasmic particles (CP), and the radial arms (RA). A weaker band of density (indented in the middle) runs vertically along the outer surface of the inner spoke ring and, at this resolution, connects the cytoplasmic and nucleoplasmic thin rings. This density may be attributed in part to the border of the nuclear envelope (M). In Fig. 4 *d*, the central domains (CS) appear to traverse this ring of density. However, structural rearrangements within the inner spoke ring may also contribute to the "membrane" density at this radius.

Color-coded surface views of the 3D map are presented in

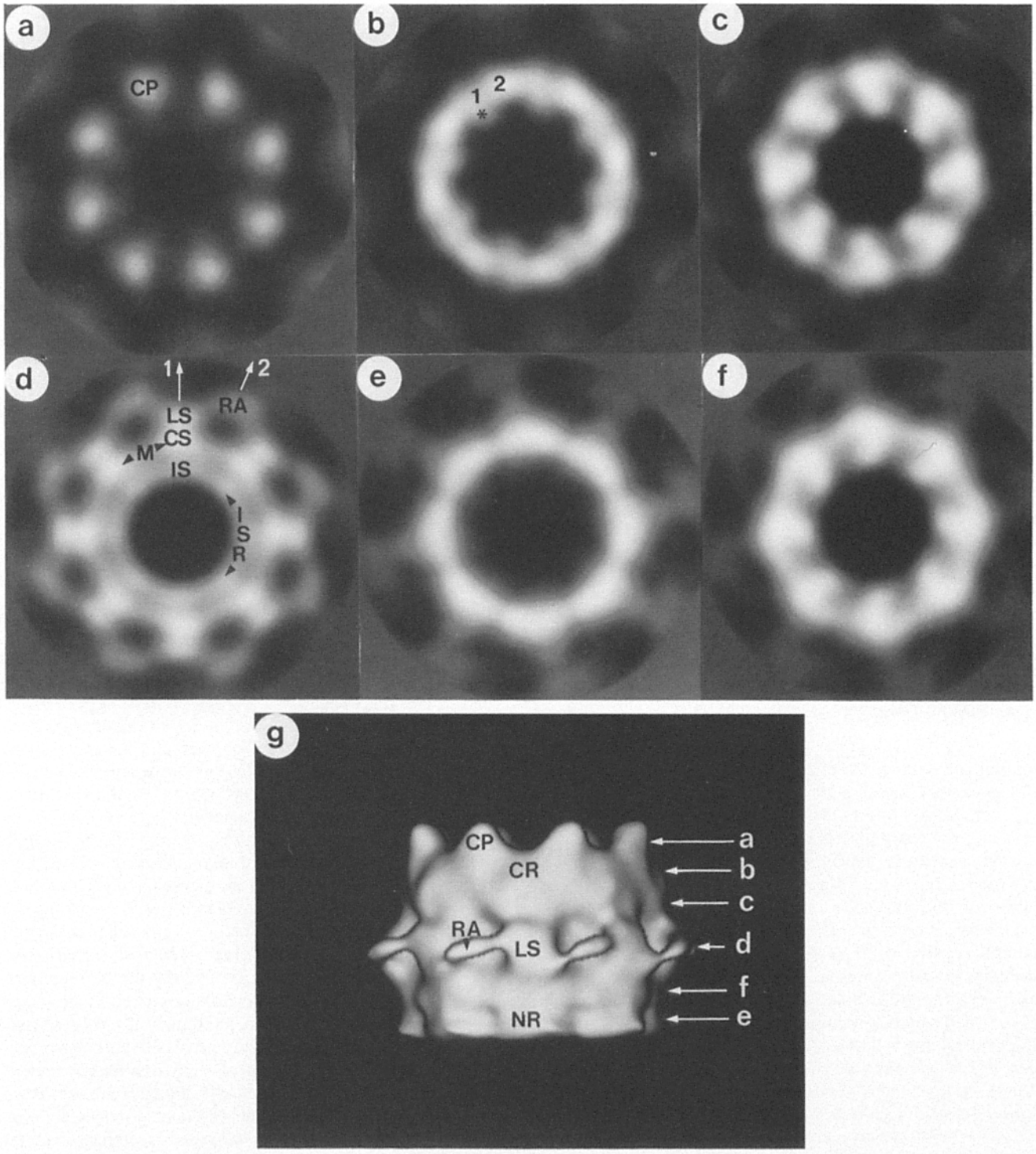

Figure 4. A montage is shown of averaged xy slices taken from the final 3D map of the membrane-associated NPC. The complete volume has 64 slices spaced 25-Å apart along the z-axis. A sideview of the 3D structure is shown in *g* as a surface model, with the slice positions and external domains indicated. This map maintains approximate twofold symmetry over most of the spoke assembly, in particular the central section (*d*) and slices in *c* and *f* show the expected twofold symmetric relationship. (*a*) Ring of cytoplasmic particles (*CP*): average of slices 13–17. (*b*) Thin cytoplasmic ring (*CR*) with two circumferential domains and a smaller inwards pointing domain (*asterisk*): average of slices 19–22. (*c*) Cytoplasmic region of the spoke assembly above the lumenal spoke domain: average of slices 26–27. (*d*) Central slice of the 3D map with the spoke and radial arm twofold axes shown (*white arrows 1* and *2*). Positions of the radial arms (*RA*), lumenal spoke domains (*LS*), membrane (*M*), central spoke domain (*CS*), inner spoke domain (*IS*), and inner spoke ring (*ISR*) are labeled. This section displays approximate twofold symmetry. (*e*) Nucleoplasmic thin ring with elongated subunits: average of slices 42–45. (*f*) Lower region of the spoke assembly that is related by approximate twofold symmetry to the slice in *c*: average of slices 37–38. (*g*) Side view of surface map showing the rudimentary cytoplasmic particles (*CP*), cytoplasmic and nucleoplasmic thin rings (*CR* and *NR*), lumenal domains (*LS*), and the diagonally bridging radial arm dimers (*RA*).

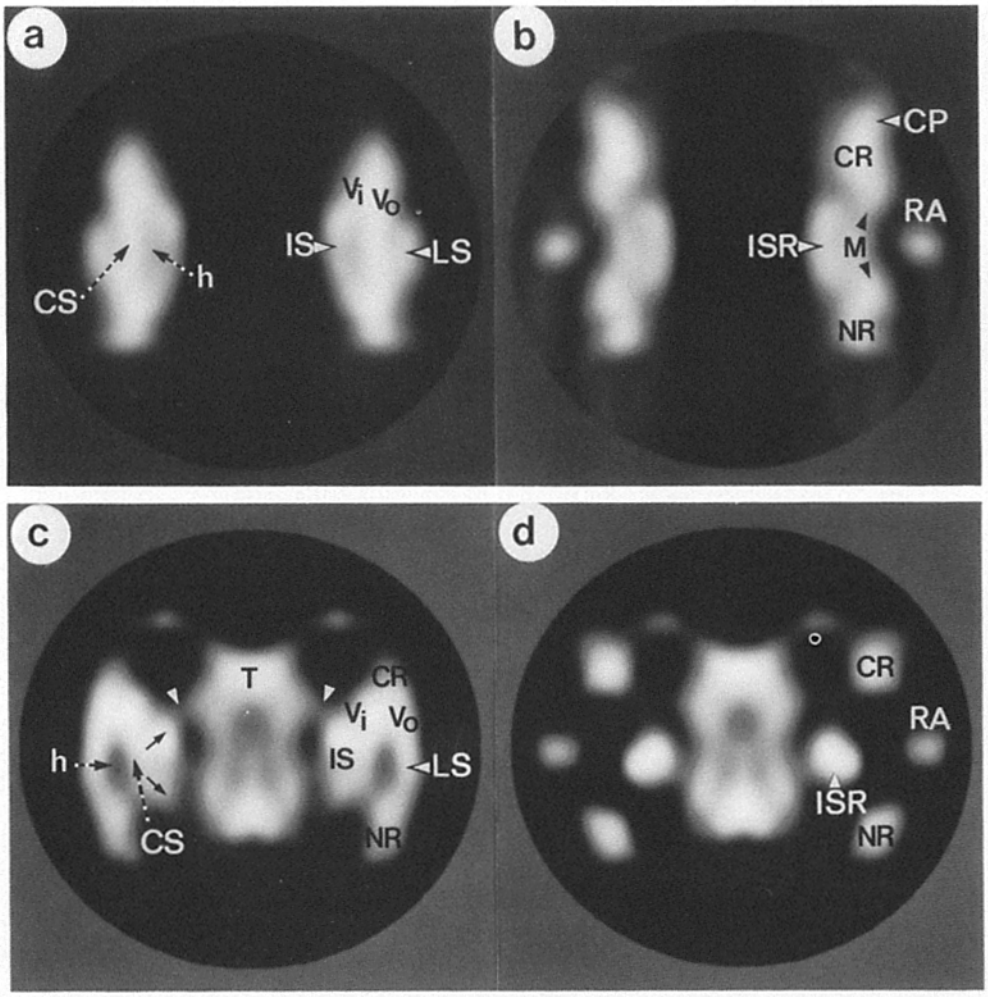

Figure 5. Cross-sections (z slices) taken from 3D maps of mform and dform NPCs after refinement by POCs/solvent flattening. *a* and *c* are slices cut along the putative spoke twofold axes; *b* and *d* are slices cut along along the putative radial arm twofold axes. *b* and *d* are related to *a* and *c* by a rotation of 22.5° around the central eightfold axis. (*a*) A z slice which bisects the spokes of the membrane-associated form is shown. Domains within the spokes are labeled including: inner spoke domain (*IS*), central domain (*CS*), lumenal domain (*LS*), the inner vertical domain (*Vi*), and the outer vertical domain (*Vo*). An area of weak interaction between the inner spoke domain and the central spoke domain is labeled (*h*). (*b*) A z slice which bisects the radial arms is shown. Additional domains are visible including: the cytoplasmic and nucleoplasmic thin rings (*CR* and *NR*), the radial arms (*RA*), the inner spoke ring (*ISR*), and the nuclear envelope border (*M*). The cytoplasmic ring and attached particles (*CP*) combine to form a cresent shape in this view. (*c*) A z slice which bisects the spokes of the detergent-extracted form is shown. Additional domains are labeled including the transporter (*T*), cytoplasmic and nucleoplasmic thin rings (*CR* and *NR*), and connections to the inner spoke ring (*white arrowheads*). Other domains labeled as above. Note that the inner spoke domain is split into cytoplasmic and nucleoplasmic domains (*small black arrows on left*) that join at the midline of the spokes and interact with the inner vertical domains and the central domain. (*d*) A z slice which bisects the radial arms of the dform is shown. Note that the membrane density is missing and the inner spoke ring is more rounded.

Fig. 6. End-on and oblique views (at 45°), as viewed from the cytoplasmic side, emphasize the connectivity of the lumenal ring (Fig. 6, *a* and *b*). Within the lumenal ring, the radial arms attach diagonally in an alternating fashion to the top and bottom of adjacent lumenal spoke domains. The spoke–ring complex is colored a medium blue while the lumenal ring is darker blue. The cut-away surfaces presented in Fig. 6, *c* and *d* are shown at a higher cutoff to minimize contributions from the nuclear envelope. In these views, the individual spokes and a dimeric splitting within the inner spoke ring are visualized.

NPCs Associated with the Nuclear Lamina after Detergent Extraction

Nuclear envelope ghosts were obtained by TX-100 extraction of nuclei, extruded into low salt buffers, and subsequently spread onto grids for rapid freezing. Under these conditions NPCs remain attached to the disordered lamina (but see references 2, 3). Areas of a zero tilt/42° tilt pair are shown in Fig. 1, *c* and *d*. The position of the tilt axis is indicated by the white arrow and the lamina is visible as a diffuse network of fine strands located between the NPCs (*black arrowheads* labeled "*L*" in Fig. 1 *c*). In general, the NPCs demonstrate a high occupancy of central ring-like transporters (*white arrowheads* in Fig. 1 *c*). Averages from 284 dform NPCs after alignment are shown in Fig. 2 *b* (untilted) and *e* (cylindrical average). The spoke–ring complex is more asymmetric than observed in the best images from *Necturus* (3) and displays the lower point group symmetry C8. The radial arms are visible between the spokes at high radius but are characteristically more diffuse than in maps of mform NPCs (3). In addition, the NPC transporter is visualized in projection as an averaged "plug" that may encompass a number of different transport-related configurations (C. W. Akey, unpublished data; see references 4, 8). Interestingly, the transporter is visible in the tilted cylindrical average as a horizontal band of density within the inner bright elliptical ring, and the cytoplasmic and nucleoplasmic thin rings are resolved (Fig. 2 *e*). Numerous attempts were made to obtain symmetrical (~822) specimens from *Xenopus* without success. A projection map from a second dform specimen is shown in Fig. 2 *c*. The similarity of the two averages suggests that this configuration is reproducible and similar maps have

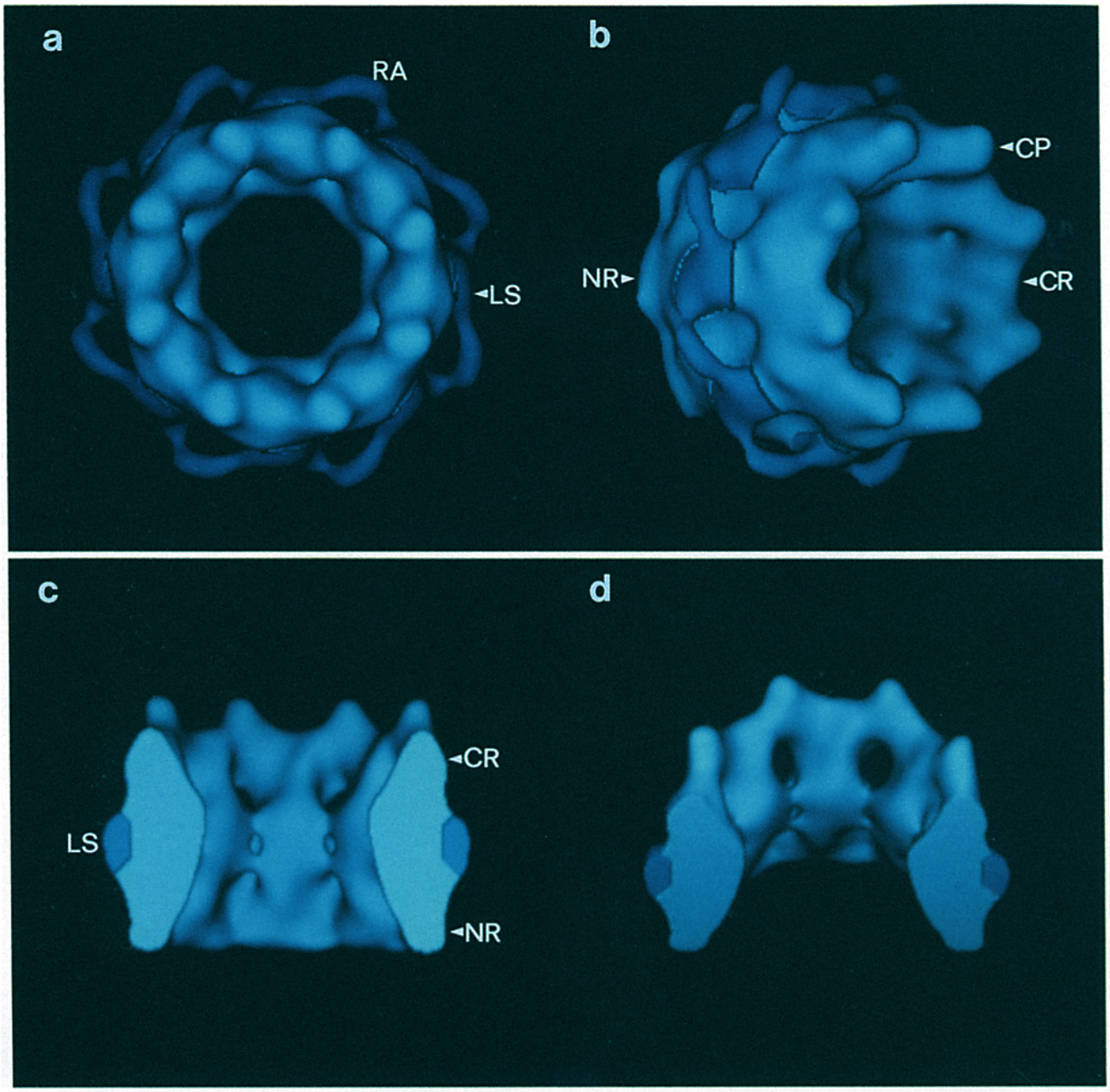

Figure 6. Surface views of the 3D map of the mform are presented at two different density cutoffs. The spoke–ring assembly is medium blue, the lumenal ring is dark blue. (*a*) The NPC is shown as viewed directly down the eightfold rotation axis from the cytoplasmic surface. The octagonal central channel formed by the inner spoke ring has a diameter of ~440 Å in this view. The lumenal ring comprised of the lumenal spoke (*LS*) and radial arm (*RA*) domains extend radially from the spokes into the lumen of the nuclear envelope. (*b*) A view of the pore complex rotated 45° about a vertical axis from the view in *a* is shown. The diagonal bridging of the lumenal domains by the radial arm dimers is shown clearly. Remnants of the cytoplasmic particles (*CP*) protrude from the cytoplasmic thin ring (*CR*) of the NPC. The nucleoplasmic thin ring is also indicated (*NR*). (*c*) A cut-away surface view of the mform NPC is shown with the cytoplasmic surface upwards. This view is shown at a higher cutoff to eliminate weaker density between adjacent spokes that is contributed in part, by the nuclear envelope. The positions of the cytoplasmic and nucleoplasmic thin rings are indicated as is the lumenal spoke domain. (*d*) The same cut-away surface is shown rotated 45° towards the viewer to show the gaps between adjacent spokes which delineate the cytoplasmic ring and the dimeric splitting that occurs in the inner spoke ring.

been obtained from negatively stained NPCs (11, 52). For comparison, a map of dform NPCs is shown in Fig. 2 *f* (n = 284) in which the pore complexes were obtained from older *Necturus* oocytes. Note that the preservation of twofold symmetry within the spokes and inner spoke ring is intermediate in character between the *Xenopus* maps and the best maps from *Necturus* (3).

Representative xy slices taken from the 3D volume of the dform NPC, equivalent to those presented from the 3D map of the mform NPC, are shown in Fig. 7. The in-plane sym-

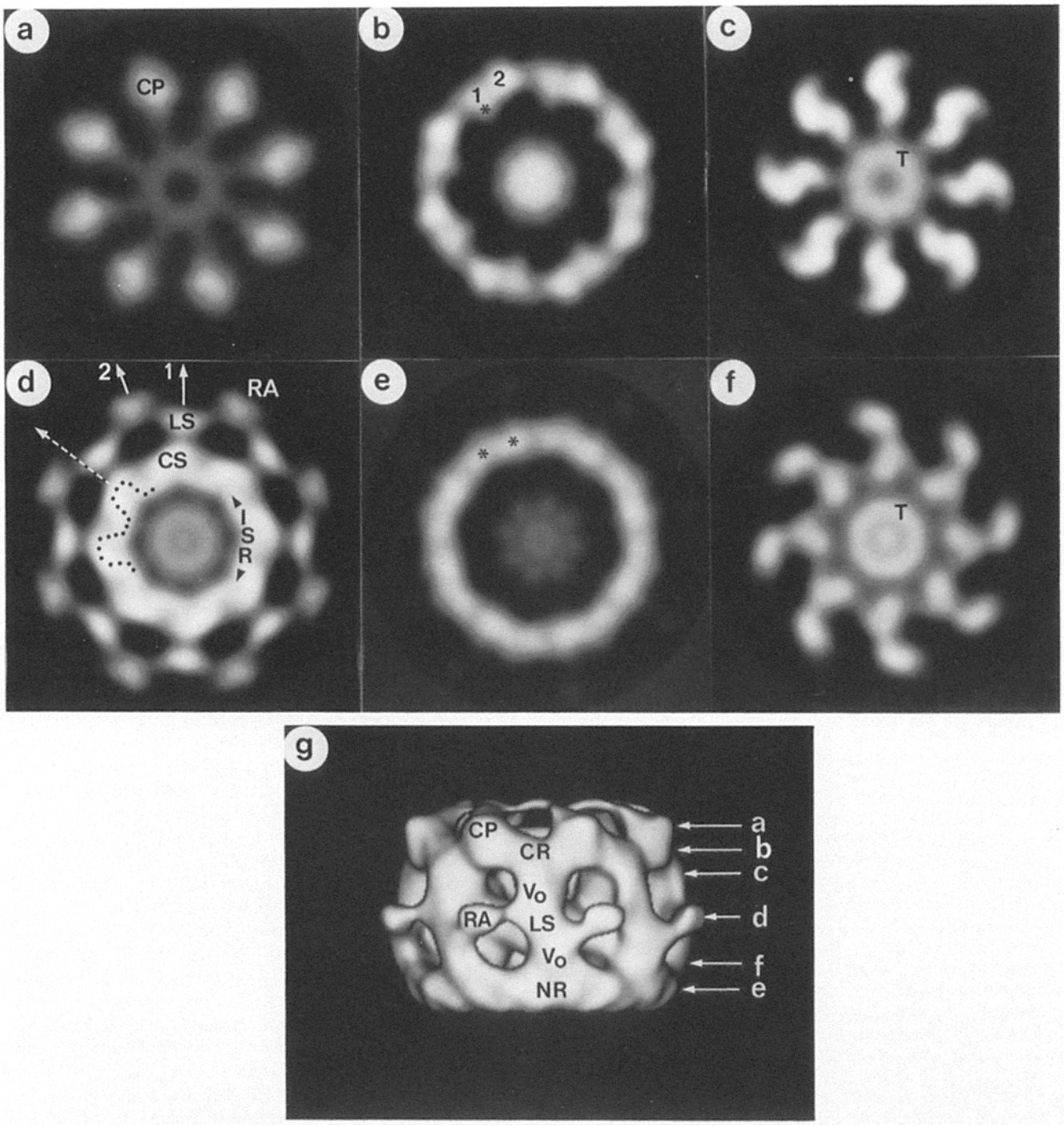

Figure 7. A montage of averaged xy slices from the 3D volume of the detergent-extracted NPC is shown. A surface model viewed from the side is included in *g* to orient the viewer. The 3D map is 64 cubed with a 25 Å spacing between xy slices along z. (*a*) Ring of cytoplasmic particles (*CP*): average of slices 17–20. (*b*) Cytoplasmic thin ring with two major domains in each ring "subunit" and a smaller inwards pointing domain (*). The very top of the transporter is visible in the center: average of slices 22–24. (*c*) The cytoplasmic region of the spoke assembly is shown. Note the left handed pinwheeling of the spoke domains. The central transporter is labeled (*T*): an average of slices 28–29. (*d*) The central section through the 3D map of the dform NPC is shown. The radial arms (*RA*), lumenal spoke domain (*LS*), central spoke domain (*CS*), transporter (*T*), and inner spoke ring (*ISR*) are labeled. This section is an average of slices 33–34. Note the local two fold symmetry of the lumenal ring about putative spoke and radial arm twofold axes (*white arrows 1* and *2*), that are repeated eight times around the cylindrical NPC. This symmetry is broken by a local twisting of the inner spoke ring and central domains which are inner-connected at this level in the map (see dotted surface). This counterclockwise twist results in the local twofold axes for the central and inner spoke domains being radially offset between the twofold axes of the lumenal ring system (dotted white arrow is offset by 45° for clarity and is flanked on either side by local symmetry axes 1 and 2 due to the eightfold rotational symmetry of the NPC). (*e*) Nucleoplasmic thin ring: average of slices 43–47. The ring displays two distinct domains marked with asterisks (*). (*f*) The nucleoplasmic region of the spoke assembly is shown, comparable to *c*. Note that the pinwheeling of the spoke domains is righthanded, in a direction opposite to *c*, as expected for a structure with approximate twofold symmetry. However, the correspondence in features between *c* and *f* is not perfect due to local disordering of the nucleoplasmic half of the NPC in this map: an average of slices 37–38. (*g*) Surface map of the dform NPC viewed from the side with the vertical positions of various slices indicated. Major domains of the spoke ring assembly are labeled: cytoplasmic particles (*CP*), cytoplasmic ring (*CR*), outer vertical domain (*Vo*), lumenal spoke domain (*LS*), radial arm dimer (*RA*), and nucleoplasmic thin ring (*NR*).

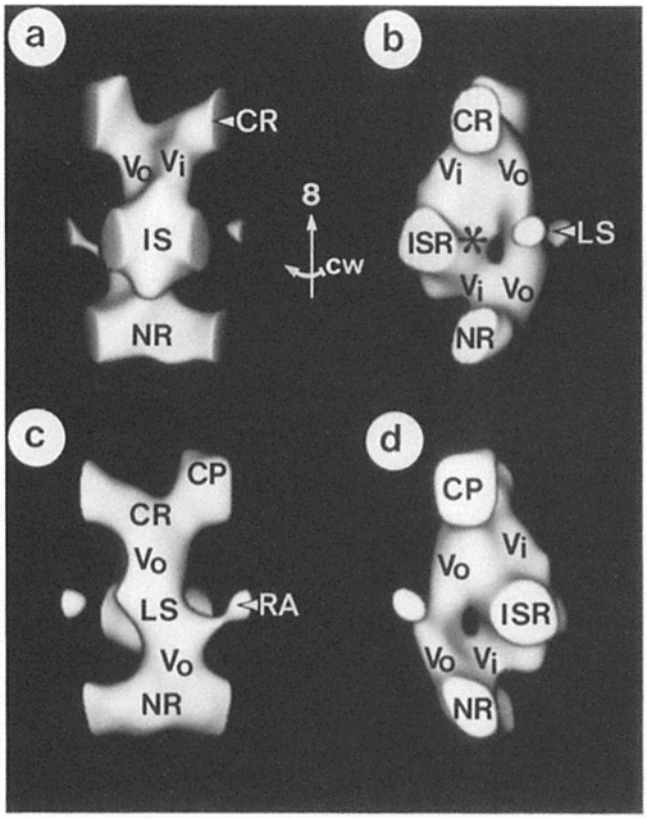

Figure 8. An individual wedge-shaped spoke from the 3D map of the dform is shown, in a rotation series. The axis of rotation is vertical and the cytoplasmic surface is at the top of each image. The direction of rotation is out of the plane of the page towards the viewer (or clockwise when viewed from the top of the figure, along the eightfold axis). Portions of the cytoplasmic and nucleoplasmic thin rings that interact with the spoke are also included. (*a*) A view from the center of the NPC showing the inner spoke domain (*IS*), inner spoke ring (*ISR*), the cytoplasmic and nucleoplasmic thin rings (*CR* and *NR*), and the inner/outer vertical domains (*Vi/Vo*). (*b*) In this view, the spoke has been rotated 100° clockwise. Note the presence of the central hollow that separates the outer vertical and the lumenal spoke domains (*LS*) from the central domain, marked with an asterisk (*). Disorder in the nucleoplasmic half of the map is manifested by the smaller volume of the inner vertical domain on the bottom surface of the spoke. (*c*) View of individual spoke–ring components from outside the NPC. This view is related to *b* by a clockwise rotation of 80°. The lumenal domain is visible and is tilted up to the left and down to the right, where it is bounded by attachments to the radial arms (*RA*). (*d*) Final clockwise rotation of 90° to complete the series. The cytoplasmic particle (*CP*) protrudes from the cytoplasmic ring. *b* and *d* present views of opposite surfaces of the wedge-shaped spoke.

metry of the central slice (Fig. 7 *d*) is more complicated than in the mform NPC. Instead of one set of approximate twofold axes there are two sets of "local" approximate twofold symmetry axes rotationally offset by ~12–15°. The first set is indicated by the white arrows labeled "*1*" and "*2*" in Fig. 7 *d* and reflects the approximate twofold symmetry of the lumenal domains and radial arms. The position of the corresponding "spoke" twofold symmetry axis in the second set (offset by 45° for clarity) is shown by the dashed arrow. This approximate twofold axis bisects the central and inner spoke domains. The local rotational distortion that gives rise to the two sets of offset symmetry axes is less marked for the inner spoke domains located above and below the central xy slice (Fig. 8 *a*). Nearly equivalent slices located above and below the midplane of the spoke complex show the spokes as "pinwheels" with opposite handedness, as expected for a structure with twofold symmetry (Fig. 7, *c* and *f*). However, the correspondence in detail between the slices is only approximate. In addition, both the cytoplasmic and nucleoplasmic thin rings have eight paired domains although the density in the nucleoplasmic rings is weaker (compare Fig. 7, *b* and *e*). Both the positions and shapes of peaks within the cytoplasmic rings of the mform and dform NPCs are similar, including the small inward pointing regions. Unexpectedly, the cytoplasmic particles are better preserved in the dform NPC (Fig. 7 *a*), due possibly to a higher occupancy after specimen preparation. Cylindrical features at the centers of the xy slices are described in the next section on the NPC transporter.

There are large and intriguing differences present in the 3D maps of the mform and dform NPCs. In comparing cross-sections from the two maps (Fig. 5, *a* and *c*), it appears that the lumenal domains extend radially to a comparable distance. Other spoke domains are present in differing orientations relative to their neighboring domains. For example, the outer rod of vertical density in the mform NPC (Fig. 5 *a*) is kinked in the dform NPC (Fig. 5 *c*) rather than straight. Moreover, two vertical domains (Vo) appear to link the lumenal domain to the cytoplasmic and nucleoplasmic rings. The outer vertical domains also may form lateral contacts with the inner vertical domains (Vi). The "twofold" related inner vertical domains connect the inner spoke domain to the cytoplasmic and nucleoplasmic rings, respectively, although the lower connection is more disordered in the map of the dform. The structural role of the central domain may be pivotal, as a radial displacement of this domain may possibly have occurred in response to relative movements of the lumenal and outer vertical domains (Fig. 7 *d*). It seems likely that mechanical distortions may have induced the observed rotational displacement of this domain from the spoke twofold axis. In addition, the inner spoke domain is a dimer of two smaller domains that are connected to the central domain by a pair of strand-like connections at the midplane of the map (dotted line in Fig. 7 *d*). These strandlike connections may move outwards in the presence of the nuclear envelope and contribute to the ring of density observed at a radius of 420–430 Å in the mform NPC.

A cross-section located 22.5° clockwise from Fig. 5 *c*, bisects the radial arms as shown in Fig. 5 *d*. A number of features in common with the mform NPC are visible including the cytoplasmic particles, the cytoplasmic and nucleoplasmic rings, the radial arms and the inner spoke ring. However, the inner spoke ring has become more rounded and the vertical density located between the spokes in the 3D map of the mform NPC is absent. This latter density is abolished after detergent extraction; hence, it may originate in part from the nuclear envelope pore in which the NPC resides. The inner spoke ring plays a critical role in maintaining the integrity of the NPC, yet is rather variable when comparing projection maps of symmetric and asymmetric dform NPCs (this work; and references 3, 34) with maps of mform NPCs (3, 4). This variability may reflect differing interactions of the inner spoke ring with the encircling nuclear envelope, as the result

of detergent extraction or specimen preparation. In addition, the thin rings in the scaled 3D map of the mform NPC are 6–10% smaller in diameter than in the dform NPC. This suggests that the thin rings may be compressed radially as the result of an inward-directed pressure associated with the nuclear envelope.

Domain connectivity within a wedge-shaped spoke is shown in a rotation series of four surface maps in Fig. 8, with the rotation axis aligned vertically. The path of strongest connectivity may run as follows: the cytoplasmic portion of the inner spoke domain connects to the ridgelike inner vertical domain, which interacts with both the cytoplasmic thin ring and the outer vertical domain. The outer vertical domain contacts the lumenal domain which is linked to adjacent spokes by radial arm dimers forming a lumenal ring. The connectivity sequence described for the cytoplasmic half of the spoke is continued around the nucleoplasmic half as shown in Fig. 8, *c* and *d*. The asterisk in Fig. 8 *b* marks the location of the central domain which is intimately associated with the inner spoke domain and rotationally offset from the spoke midline. The surface morphologies of the spoke ring assembly presented in this report and the 3D map described by Hinshaw and co-workers (34) are similar but not identical. Importantly, comparisons between maps of distinct but related forms have allowed us to make a qualitative assessment of domain connectivity and potential flexibility, after compensating for disorder within the nucleoplasmic halves of our 3D maps.

Color coded surface maps of the dform NPC structure are presented in Fig. 9 (*a–f*). The color coding is as follows: the lumenal ring is dark blue, the spoke–ring complex is medium blue and the transporter is pink. As with the mform NPC, the radial arm dimers connect lumenal domains in adjacent spokes to form a lumenal ring of nucleoporins (Fig. 9, *a* and *b*). Furthermore, the lumenal domain does not protrude from the spoke as strongly but rather is more closely in contact with the outer vertical domains located above and below it (Fig. 9, *b* and *c*). Eight large particles are associated with the cytoplasmic ring. Their outermost portions mediate attachment to the cytoplasmic thin ring (Fig. 9 *c*) while the innermost regions are linked by a weak ring of density (Fig. 9, *a* and *b*). This ring was not observed previously but may represent cytoplasmic filaments that have collapsed onto the NPC as the aqueous buffer layer thins during specimen blotting.

A surface map of the dform NPC in which the transporter and half of the spoke–ring complex have been computationally removed is shown in Fig. 9 *d*. In this view the alternating sizes of the domains which comprise the inner spoke ring are visible as are the cytoplasmic and nucleoplasmic thin rings. The inner spoke domain is tilted ~7° clockwise from the vertical axis, towards the cytoplasmic surface and is comprised of two sub-domains related by an approximate twofold axis. The inner and outer vertical domains connect the thin rings to the inner spoke ring and outer portions of the spokes, respectively. These domains are emphasized by the small hollow feature that radially separates the lumenal domain from the inner spoke ring/central domain (Fig. 9, *d–f*). Moreover, the observed rotational displacement of the central domain within the spoke may have accentuated the size of the hollow. This feature was not visualized in negatively stained NPCs, possibly because specimen compression associated with drying (~35–50%) may have closed this small hollow (see reference 34).

The NPC Transporter: A Tripartite Cylindrical Assembly

The NPC transporter was not preserved in specimen used to calculate the 3D map of the mform NPC; therefore, this map has a large central channel. However, the central transporter is present at a very high occupancy (~75–80%) in the dform NPCs. A corresponding ring of density is observed at the centers of the xy slices within the 3D map (Fig. 7, *b–e*), and depending on the level within the map this ringlike feature is either hollow or appears to be partially occluded by "endogenous" material. A different perspective is obtained by viewing the cross-sections shown in Fig. 5, *c* and *d*. In these z-slices, the NPC transporter is centrally tapered giving the impression of a tripartite structure constructed with very approximate twofold symmetry. The transporter appears to be hollow but additional density is present in the nucleoplasmic half of the map. This axial material may represent an averaged view of substrates caught "in transit" within the transporter (4, 8), coupled with residual noise peaks. The trapping of substrates during enucleation into buffers without ATP may occur rather readily (3, 8), as transport through the NPC is probably a highly cooperative process that requires soluble factors and ATP (1, 44, 46).

The cytoplasmic and nucleoplasmic surfaces of the transporter appear solid; a central channel entrance is not present. It cannot be ascertained if this is an intrinsic feature of the transporter or alternatively, may reflect the average super positioning of substrates docked at entrances to the central transport channel (4, 8). The external tapering of the transporter cylinder is mirrored internally. The channel diameter is ~90Å wide at the waist and expands out to 110Å in the cytoplasmic half and 160Å in the nucleoplasmic half of the transporter. To some extent, these differences may reflect the presence of the axial material in the nucleoplasmic half of the transporter. The walls of the transporter are thinnest at the central taper, ~75–90Å. These estimates will change with the collection of improved data on NPCs with defined configurations, as partial occupancy of substrates within the transporter may cause the walls to appear thicker after rotational averaging. Interestingly, the small diameter of the putative transport channel at the central waist would suggest that this region, located between possible gating assemblies at either end, may be flexible and undergo considerable expansion during substrate translocation (17, 61).

In surface views of the NPC, the transporter appears as a central protruding cylinder with a flat cytoplasmic surface (Fig. 9, *a–c*). The complete transporter is revealed as a tripartite hourglass-shaped cylinder with an axial dimension of ~625Å, in views in which half of the spoke–ring assembly has been computationally cut away (Fig. 9, *e* and *f*). The central waist of the transporter is ~320Å in diameter while the putative gating assemblies located at either end have maximal diameters of ~420Å. The transporter in this structure is a global average of at least three to four different configurations that may be transport related (unpublished data); hence, additional data and classification analysis will be needed to resolve individual domains or subunits within the assembly. Connections between the transporter and the inner

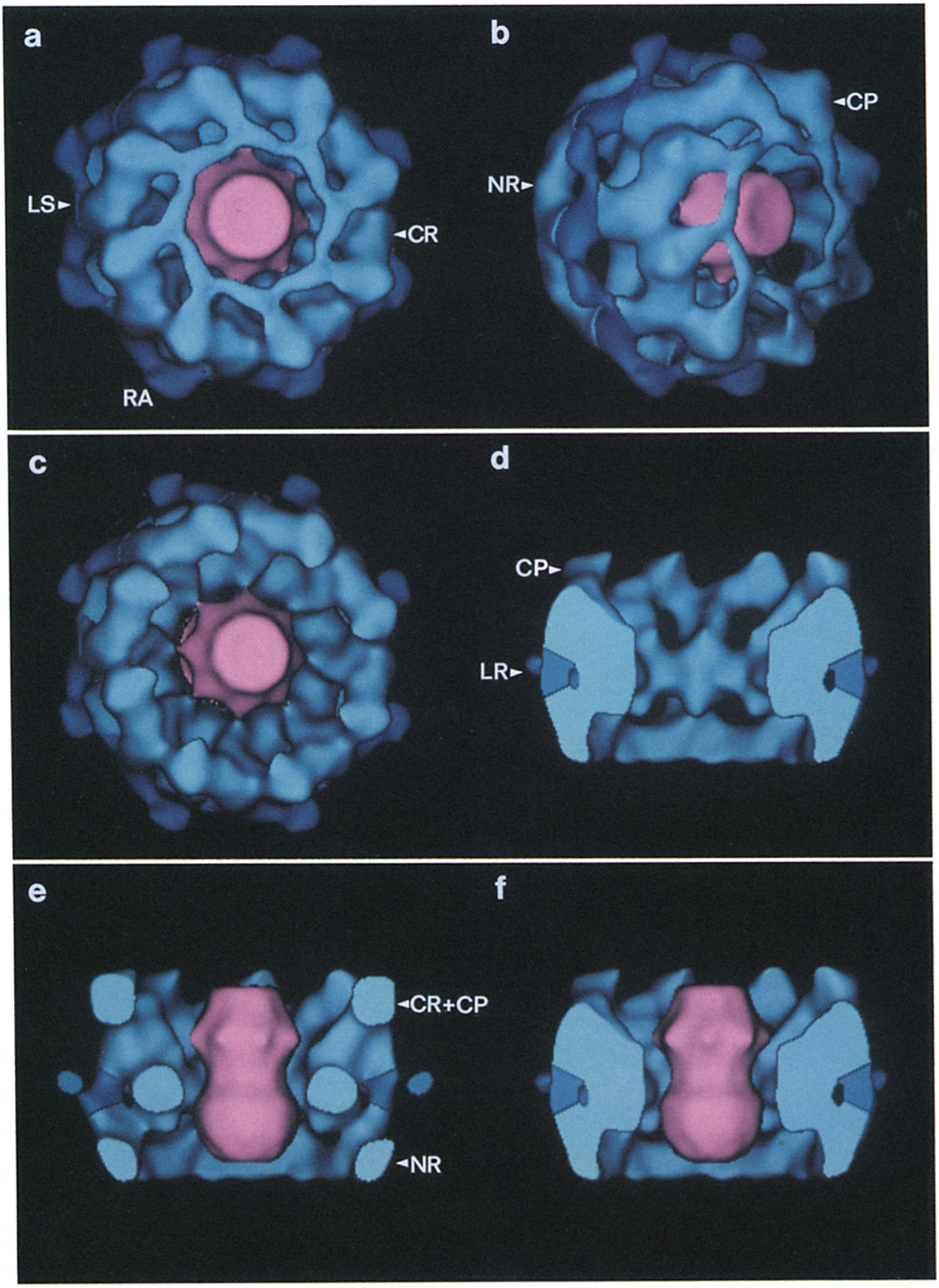
a
LS
CR
RA
b
CP
NR
c
d
CP
LR
e
CR+CP
NR
f

spoke ring form a set of eight inter-connected channels (Fig. 9, *a–c*). The general shape of these channels can be seen in Fig. 9 *e*, which is shown at a higher density cutoff such that the connections between the transporter and the spoke-ring assembly are eliminated. These internal channels were observed previously in projection, in class averages of mform NPCs with central transporters (4). The channel cross-sections are roughly the correct size (80–90Å) to allow diffusion of ions, small molecules, and small nonnuclear proteins across the pore complex (49). Finally, the NPC-transporter is vertically displaced by roughly 50Å towards the cytoplasmic surface of the NPC, away from the center of the spoke assembly (Fig. 9, *e* and *f*). This displacement may have occurred as the cumulative result of mechanical stresses during isolation; similar forces may have induced the observed asymmetry between the top and bottom halves of the spokes (see Figs. 8 and 9 *e*).

We maintain a high degree of confidence in the global structure of the NPC-transporter. First, 3D maps computed from half and quarter datasets are similar. Second, the size of the two globular end domains within the transporter, coupled with the approximate twofold symmetry, suggests that each transporter may be capable of splitting into "half-transporters" equivalent to the ~360Å diameter pluglike particles obtained during disassembly studies (62). Third, the 3D map suggests that the central, disordered cylindrical rod of density observed previously in an initial 3D map (62) may be equivalent to the transporter. Fourth, Np-gold (23) and mRNPs (28, 40, 61) share a similar topology during transport, as both substrates are restricted to a central channel that spans the entire NPC. These data are explainable in terms of the NPC transporter which may provide a macromolecular channel that traverses the entire NPC.

Discussion

A detailed molecular analysis of the structure and function of the NPC has proven difficult due in part to the size, complexity and low abundance of this intracellular leviathan (39). However, our knowledge has increased in parallel with the development of techniques to visualize and quantitatively analyze the pore complex, in combination with newer methodologies which are now allowing the biochemical and genetic identification of constituent nucleoporins. Furthermore, the approach of combining cryo-electron microscopy and X-ray diffraction analyses with biochemical and genetic information is proving to be a powerful tool in the functional dissection of large macromolecular assemblies (35, 60, 63). As a first step in understanding the dynamics of NPC conformation and function, we have used cryo-electron microscopy and single particle 3D methods to analyze the structure of NPCs associated with either the nuclear envelope or detergent-extracted nuclear ghosts. To a first approximation, the NPC proper can be described in terms of the spoke–ring complex and the central transporter (but see Fig. 11). In our experience, both assemblies may exhibit differing conformations or configurations in isolated specimen (3, 4) and we fully expect that some of these changes may be induced by sample isolation and preparation for EM. However, it is our working hypothesis that both the apparent conformational flexibility of the spoke–ring complex (3) and the observed configurations of the transporter (4, 8) may be relevant in a fundamental way to processes that occur in vivo.

Conformational Flexibility and a Minimal Domain Model of the NPC

A comparison of the two 3D structures reported in this work reveals that the spoke–ring complex may be rather flexible and allows a qualitative analysis of domain positions and interactions. Idealized domain models for the m- and dforms of *Xenopus* NPCs are shown in Fig. 10, redrawn from density maps of z-slices cut along the putative "spoke" (Fig. 10, *a* and *c*) and "radial arm" twofold axes (Fig. 10, *b* and *d*). Inferred positions of the nuclear envelope and the NPC transporter have been indicated in Fig. 10, *a* and *b*. The spoke assembly is twofold symmetric about the midplane of the structure as shown in the best 2D maps (3, 4, 42, 62) and in a recent 3D map of negatively stained NPCs (34). Although there are varying degrees of distortion present in the nucleoplasmic halves of our 3D maps, the major features support this interpretation. Inspection of the two 3D maps suggests that conformational changes involving the spoke domains and thin rings have occurred, possibly as the result of detergent-extraction, osmotic shock within the lumen of the nuclear envelope or mechanical stresses during specimen preparation.

As an aid in visualizing the overall design of the NPC, a 3D ribbon diagram of the membrane-associated NPC is shown in Fig. 11. In addition, this diagram includes peripheral assemblies visualized by other methods that form part

Figure 9. A gallery of color coded 3D surface views is shown of the detergent-extracted NPC. The spoke–ring assembly including cytoplasmic particles (*CP*) is medium blue, the lumenal ring is dark blue and the central NPC-transporter is pink. (*a*) The NPC is shown from the cytoplasmic surface viewed at a glancing angle of 10°. Note the attachments between the transporter and the surrounding spoke ring assembly and the thin ring of density which links up adjacent cytoplasmic particles. The lumenal spoke, radial arm domains and the cytoplasmic thin ring are labeled. (*b*) A view of the NPC rotated 45° about a vertical axis is shown. The lumenal ring is highlighted in this view. The cytoplasmic particles and the nucleoplasmic thin ring are labeled. (*c*) A view of the NPC from the cytoplasmic surface is shown in the same orientation as *a*, but with the top portion of the cytoplasmic particles removed to show the packing of the transporter within the inner spoke ring. Entrances to possible diffusion channels are delineated by the connections between the transporter and the inner spoke ring. (*d*) A cut-away view of the spoke–ring assembly is presented with the central transporter removed to show the internal surface of the spoke–ring assembly. The cut was made along the approximate spoke twofold axis which bisects two of the wedge-shaped spokes. The lumenal ring and the cytoplasmic particles are indicated. (*e*) A second cut-away view is shown with the transporter left intact. In this view the cutting plane is oriented along a putative radial arm twofold axis, between adjacent spokes. The packing of the transporter within the wedge-shaped spokes is visible as are opposite surfaces of the spokes (compare with Fig. 8). (*f*) A cut-away side view of the NPC is shown in the same orientation as *d* with the transporter left intact. Internal channels located between the hourglass-shaped transporter and the inner spoke ring are revealed. The transporter spans the width of the NPC and the local twofold axis of the transporter is offset from the approximate twofold axis of the spoke–ring assembly by ~50 Å, towards the cytoplasmic/top surface.

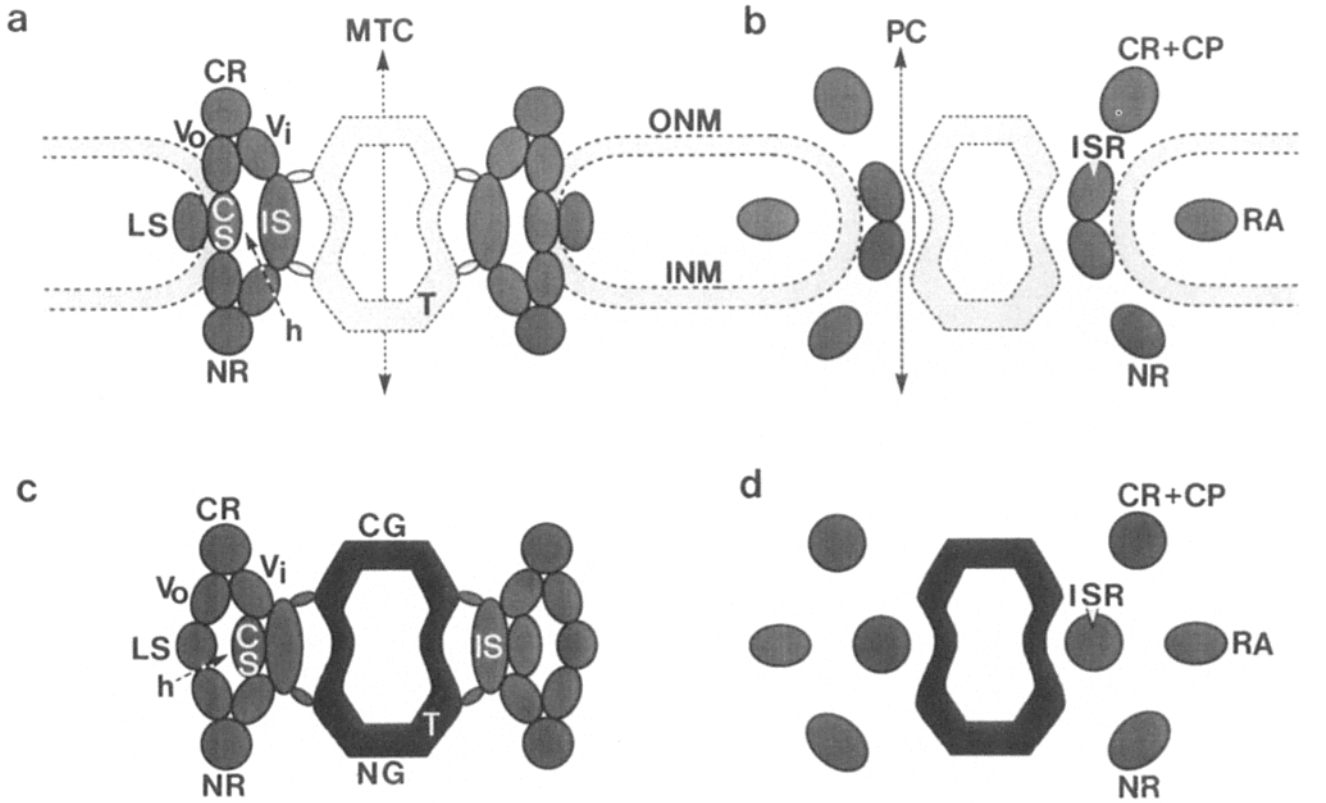

Figure 10. Diagrammatic cross-sections are shown of the membrane-associated and detergent-extracted NPCs. Peripheral assemblies like the cytoplasmic filaments and nucleoplasmic cages have been omitted for clarity. The density maps presented in Fig. 5 and other data were used to deduce a minimal domain model. In addition, this analysis allowed conformational rearrangements involving the lumenal spoke domain, the outer vertical domains and the central spoke domain to be deduced. The diagrams have been idealized by enforcing exact twofold symmetry about the membrane plane for the spokes. The cytoplasmic and nucleoplasmic rings are not presumed to be identical and the central hollow in the spokes has been exaggerated for clarity. The diameter of the spoke ring assembly excluding the radial arms is ~1,200 Å. The domain designations are: inner spoke domain (*IS*), inner spoke ring (*ISR*), cytoplasmic and nucleoplasmic thin rings (*CR* and *NR*), inner and outer vertical domains (*Vi/Vo*), central spoke domain (*CS*), lumenal spoke domain (*LS*), transporter (*T*), putative cytoplasmic and nucleoplasmic gating assemblies (*CG/NG*), radial arm dimers (*RA*), cytoplasmic particles (*CP*), and inner and outer nuclear membranes (*INM* and *ONM*). (*a* and *b*) Z slices from the mform map are shown, cut along putative twofold axes aligned with the spokes and the radial arms. The nuclear envelope and NPC transporter are shown superimposed onto their approximate locations (features shown with dotted lines and lighter shading). Note that the vertical rod of density within the spoke in Fig. 5 *a* has contributions from the nuclear envelope, as well as the central and the outer vertical domains. The lumenal spoke domain and the radial arms protrude into the lumen of the nuclear envelope. This model predicts the existence of more than one type of membrane spanning protein within the pore complex. Possible positions of the macromolecular transport channel (*MTC*) and the passive diffusion channels (*PC*) are indicated by vertical dashed lines in *a* and *b*, respectively. (*c* and *d*) Idealized z slices are shown for the 3D map of the dform. The size of the cavity located between the inner spoke/central spoke domains and the lumenal spoke domain has been exaggerated (*h*). In addition, connections between the transporter and the nucleoplasmic face of the inner spoke domains have been included although they are weak in the original map, due to local disorder. Note the overall change in shape of the inner spoke ring in *b* and *d*, which suggests that the nuclear envelope has a significant effect on the conformation of this structural element.

of the extended model of the NPC (2, 28, 33, 36, 55, 57). Individual domains have been reduced in size (or in some instances omitted) for clarity; for example the inner spoke ring has been reduced in height to allow visualization of the central NPC transporter. However, this reduction causes a distortion of the inner vertical domains within the wedge-shaped spokes. Hence, the ribbon diagram should be used to orient the various subassemblies of the NPC, the model cross-sections in Fig. 10 are more accurate in terms of the spatial relationships between spoke domains. Simply, the architecture of the spoke–ring assembly can be described in terms of four colinear rings, that use homologous and heterologous interactions between domains to maintain the integrity of individual spokes while mediating assembly of the eightfold symmetric pore complex. First, the inner spoke ring is formed by domains that bridge the inner domains within adjacent spokes to form an eightfold symmetric annulus. The inner spoke ring appears to be the central organizing element of the spoke–ring complex and may function as an adaptor between the spoke–ring complex and the NPC transporter, to which it is connected (Fig. 11). Second, the cytoplasmic and nucleoplasmic thin rings may stabilize the spoke–ring assembly by making intimate contacts with the inner and outer vertical domains in each of the eight spokes. Third, the anchoring of the spoke assembly within the nuclear envelope may be stabilized by the formation of a lumenal ring, comprised of eight lumenal domains bridged by radial arm dimers (Fig. 11). Importantly, the position of the

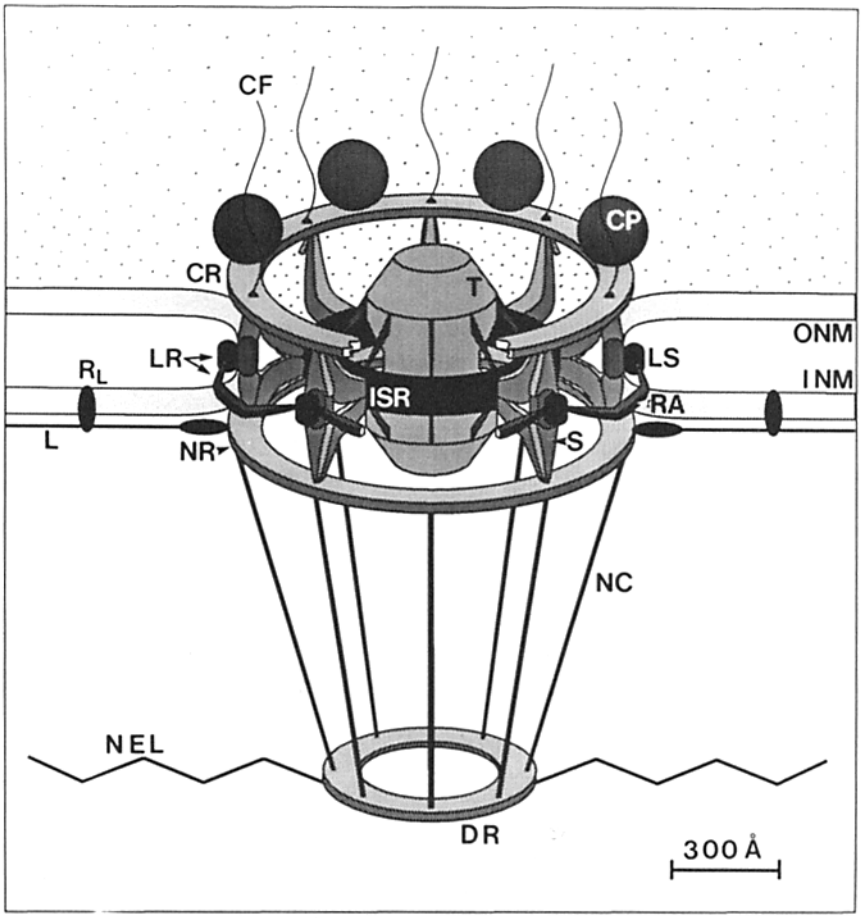

Figure 11. A 3D representation of the membrane-associated NPC is presented as a ribbon diagram. Structural information from other groups has been incorporated to give an overall impression of our current knowledge of the extended architecture of the NPC (2, 28, 33, 36, 55). For clarity, the dimensions of certain features have been minimized and the top cytoplasmic ring (*CR*) is sliced open to reveal the interior. For example, the inner spoke ring (*ISR*) is shorter and thinner than in the real structure (see Fig. 9, *d-f*). These changes result in some artistic adjustments being made in the shape of the inner vertical spoke domains which link up the ISR to the cytoplasmic thin ring. The spokes are wedge shaped with seven domains in the diagram. In actuality the inner spoke domains (part of the ISR in this diagram), the central and the lumenal domains are dimers, giving a total of 10 domains per spoke. The diagram emphasizes the construction of the NPC from four collinear ring systems including the cytoplasmic and nucleoplasmic thin rings (*CR/NR*), the inner spoke ring (comprised of the inner spoke domains and the material between spokes) and the lumenal ring which links up adjacent spokes within the lumenal space. The lumenal ring is composed of the lumenal domains (*LS*) and the radial arm dimers (*RA*). Additional components of the NPC proper are labeled: cytoplasmic particles (*CP*), the spokes (*S*), and the tripartite transporter (*T*). The precise attachment sites of peripheral assemblies are not known. Cytoplasmic components include thin filaments (*CF*) which attach to the exposed thin ring and the outer nuclear membrane (*ONM*). On the nucleoplasmic surface, the lamina is apparently anchored into the inner nuclear membrane (*INM*) by a membrane receptor (R_L). An octagonal cage or basketlike structure (*NC*) is attached to the outer surface of the nucleoplasmic thin ring. This structure may extend ~1,000 Å into the nucleoplasm. Moreover, adjacent NPCs may be linked into groups by the nuclear envelope lattice (*NEL*) which interconnects distal rings (*DR*) of the cages (33). Finally, thin bridges of material connect each half of the transporter to the inner spoke ring, thereby forming a set of interconnected channels that may share a common vestibule formed by the packing of the centrally tapered transporter within the inner spoke ring.

central domain within a wedge-shaped spoke may be pivotal, as this domain appears capable of moving ~35–40Å radially in a rearrangement that may involve a repositioning of the outer vertical and lumenal domains (compare *a* and *c* in Fig. 10). Overall, the dimeric inner spoke, central, and lumenal domains each contribute a domain to the vertical inner and outer domains to form half of a wedge-shaped spoke with a total of five domains. Subsequently, each half spoke is paired about a central twofold axis (3, 34, 42) to generate a complete spoke and eight of these units combine with the cytoplasmic and nucleoplasmic thin rings to form an articulated spoke–ring assembly.

A comparison of the 3D map of *Xenopus* NPCs reported by Hinshaw and co-workers (34) with our work, reveals that the basic features of the spoke–ring complexes are remarkably similar including a sharing of the same absolute handedness. The 3D maps of both dform NPCs were produced using the random conical tilt reconstruction method (50), with different image processing packages (SPIDER/SUPRIM) and different specimen preparative methods (frozen-hydrated specimens vs. negative-staining). The similarity of the final 3D structures serves to validate both the 3D reconstruction methods and the reliability of the resulting maps. Although rapid freezing can potentially preserve structural order to atomic resolution, specimen dependent factors generally result in a much lower attainable resolution. For example, the nucleoplasmic halves of the 3D maps may be partially disordered resulting from the transduction of mechanical stress along the fibrous lamina and its attachments to the NPC (2,3). Alternatively, changes in spoke–ring conformation may result from hydration changes of the nucleoplasm (swelling), enucleation, and the possible loss of lumenal components.

Cytoplasmic Particles and Peripheral Assemblies

Fingerprinting experiments first demonstrated the existence of asymmetrically shaped particles on the cytoplasmic surface of the NPC with a diameter of ~220Å (62). Subsequently, Reichelt and co-workers (52) measured particles released from the nuclear envelope with diameters of 230–270Å and showed them to have a mass of ~6–6.7 Mda. These particles were associated with the thin rings in some instances; however, their mass appears to preclude them

from being ribosomes. Particles are found associated with the surface of the cytoplasmic thin rings in both 3D structures presented in this work. The particles in the map of the dform are better preserved and have dimensions of ~230 × 160Å when viewed along the eightfold axis from the cytoplasm. The shape of the particles is similar to particle profiles observed in negatively stained specimens obtained by fingerprinting (62), suggesting that these are true particles rather than collapsed filaments (36, 55). At a lower density cutoff, a thin ring appears to inter-connect the eight cytoplasmic particles in the dform NPC. This ring may originate from the collapse of thin cytoplasmic filaments during adsorption of the specimen to the carbon film (33, 55). Other peripheral assemblies including the nucleoplasmic cages/baskets (33, 36, 54, 55, 57), the nuclear envelope lattice (33) and attachments to the nuclear lamina were not retained during specimen preparation or alternatively, were too strongly disordered to be visualized (see Fig. 11 for the relative positions of these components).

Interactions with the Nuclear Envelope

The NPC resides within a pore in the nuclear envelope formed by the fusion of the inner and outer nuclear membranes. In the current 3D map of the mform NPC, the nuclear envelope appears to conform to the spoke–ring assembly while spanning exposed lateral surfaces of the spokes between the two oppositely facing thin rings. In addition, the ring of density observed in projection maps of the mform NPCs, occurs at an average radius of 420–430Å in the 3D map and the central spoke domain traverses this feature. Finally, the lumenal spoke domains and the radial arm dimers form a ring of nucleoporins on the lumenal side of the nuclear membrane. We suggest that this lumenal ring may play a role in both the assembly and anchoring of the pore complex. Gp-210 a membrane glycoprotein component of the NPC with a single transmembrane domain has been proposed to play a role in anchoring the NPC to the nuclear envelope (32, 64). The 3D map of the mform NPC suggests that the large lumenal domain of gp-210 may be localized to either the radial arms or the lumenal domains. In either case, the possibility exists that the lumenal portion of gp-210 may mediate the formation of homodimers, although this species may not be stable when the molecule is removed from the context of the spoke–ring assembly.

Recently, Greber and Gerace (31) have shown that microinjection of total hybridoma mRNA encoding a gp-210 specific IgG (RL27) into tissue culture cells, results in the synthesis and transport of antibody into the lumen of the ER and the nuclear envleope, where it binds gp-210. Remarkably, the nuclear import of micro-injected nucleoplasmin was reduced fourfold and diffusion of a 10-kD dextran was also diminished in these cells. What is the structural basis for this dramatic down regulation of active transport and diffusion from the lumenal side? Depending on the location of the epitope recognized by RL27, the functional effect(s) induced by antibody binding would have to be propagated over a radial distance of ~350–520Å, to impinge on the putative diffusion and macromolecular transport channels. Although of non-physiological origin, the plasticity of the spoke–ring assembly observed in our maps may mimic certain aspects of a possible "conformational signaling" mechanism in which nucleocytoplasmic transport is globally regulated by signals originating from the lumenal side of the pore complex. For example, it is conceivable that RL27 binding to the lumenal ring may trigger rearrangements within the outer vertical and lumenal domains, which in turn are transmitted to the inner spoke ring by radial displacement of the central spoke domains. Of course, alternative routes are possible. However, the inner spoke ring may play a critical role in this scenario, as it makes connections to the NPC-transporter that define an internal network of channels. Therefore, it is conceivable that changes within the spoke–ring complex may be transmitted to putative gating assemblies within the central transporter by way of the inner spoke ring. Overall, our observations on the conformational plasticity of the spoke–ring complex in vitro, lend support to the emerging hypothesis that the spokes may transduce signals provided by as yet unidentified lumenal or intracellular effectors, thereby modulating global transport properties of the NPC under physiological conditions (22, 31).

Internal Diffusion Channels

Micro-injection studies with dextrans (49) and polyvinylpyrrolidone-coated gold particles (20) have established that diffusion channels with a limiting diameter of ~90–100Å may be present in the pore complex, resulting in an estimated transport cutoff for non-nuclear proteins and small molecules of ~40 kD. The 3D map of the dform NPC suggests that 8 diffusion channels may be located internally between the inner spoke ring and the central NPC transporter, with 16 entrances (eight from either side) delineated by connections between the transporter and the inner spoke domains (Fig. 10, *a* and *b*). The 16 entrances may link up in a common cylindrical vestibule created by the packing of the centrally tapered transporter within the surrounding inner spoke ring. A clearer picture of this internal channel network should emerge with higher resolution data on a defined transporter configuration. Recently, eight possible diffusion channels have been hypothesized by Hinshaw et al. (34) to occur between adjacent spokes at a radius outside the inner spoke ring. Our current 3D map of the mform NPC in vitro does not directly support this proposal. However, it is conceivable that the nuclear membrane may bulge outwards between adjacent spokes in vivo while remaining tethered to the central spoke domains, thereby creating "peripheral" diffusion channels for soluble and membrane proteins between the spokes. Additional experiments are needed to determine the radial position(s) of diffusion channels within the NPC in vivo.

The NPC Transporter and Models of the Translocation Step

Previous work in projection has established that a central ringlike structure is present within the NPC. This assembly has been named the transporter, as it appears to define the macromolecular transport channel for NP-gold conjugates and endogenous substrates (3, 4, 8). In this work, the 3D map of the dform NPC demonstrates a central cylindrical feature that may represent a "global" average of transporters trapped in a number of transport-related configurations during enucleation. Interestingly, the averaged transporter has a tripartite structure and is comprised of two "globular" assemblies which join face-to-face about an approximate twofold axis to form a cylinder with a tapered center. The NPC

transporter is hollow with 75–90Å-thick walls and a total length of 625Å. Studies of the nuclear import of karyophilic proteins suggest that nuclear import occurs within a central channel of the NPC as follows. Initially, microinjected substrates accumulate at the nuclear periphery in a temperature independent fashion, ATP-dependent vectorial translocation then ensues after substrate binding to the NPC (46, 47, 53). Further mapping studies using nucleoplasmin–gold have suggested that transport involves substrate docking to the central NPC transporter, before a possible gating event within this assembly (8).

A number of models for the translocation step in nucleocytoplasmic transport have been discussed. For instance, it has been suggested that substrates might move along filaments postulated to traverse the NPC aided by an ATPase/motor molecule (10). Recent data have confirmed observations that filaments are attached to both the cytoplasmic and nucleoplasmic surfaces of the NPC (33, 36, 53, 55, 57). However, our maps suggest that there is no physical room for filaments to traverse the NPC itself when the transporter is present; hence, this mode of translocation would appear unlikely. A second model has posited that a substrate bearing container may transit through the center of the spoke assembly, thereby providing protection for mRNPs. This model was recently brought to the forefront with the suggestion that vaults, a large assembly with 822 symmetry, might be involved in transport (37). However, images in which large mRNPs (28, 40, 61) and Np-gold (23) are caught transiting the entire width of the NPC would argue against the transport container hypothesis. Moreover, a container mechanism appears unnecessary as many mRNPs spend a large fraction of their lifetimes associated with fibrous tracts (reviewed in reference 38). Finally, the dimensions of the vaults and the NPC transporter in frozen-hydrated specimens are dissimilar (vaults: 490 × 275Å; transporter: 625 × 420Å) and their morphologies are rather different.

The recent visualization of octagonally arranged baskets or cages on the nucleoplasmic face of the NPC has sparked interest in the possible roles of these structures in transport (33, 36, 54, 55). However, the strict localization of the cages on the nucleoplasmic side of the NPC would pose a topological problem to possible roles in a bidirectional gating mechanism. In addition, recent micrographs of the nucleoplasmic surface of metal-coated amphibian oocytes have demonstrated the presence of a filamentous lattice that interconnects adjacent cages at their distal rings (33). Perhaps, the cages provide access to the nucleoplasmic face of the NPC transporter for macromolecules within the context of the high density of peripheral chromatin and the thickened lamina present in many cells.

Labeling studies with WGA and MAb414 suggest that the transporter may be eightfold symmetric, as these bivalent probes often label individual transporters in groups of four (8, 57). A direct determination of the symmetry of the transporter must await monospecific FAbs for components of the transporter. Recently, a macromolecular lock/double iris hypothesis has been proposed to describe the translocation of substrates catalyzed by the NPC (4). In this model the transporter is proposed to have ~822 symmetry (reviewed in references 5 and 6). The limited number of NPCs in our dataset coupled with the apparent admixture of differing transporter configurations, results in a globally averaged view of the transporter that does not allow a direct confirmation of the irislike gating mechanism at this stage. However, the tripartite morphology of the NPC transporter when combined with data on substrate translocation through the centers of NPCs (4, 8, 23), lends support to the hypothesis that this process may involve two oppositely facing gates. In this model, the two globular end domains of the NPC transporter would correspond to possible gating assemblies. It is suggested that these putative gates may open asynchronously to regulate transport along a central channel like a macromolecular lock (4, 7). Furthermore, it is tempting to speculate that the translocation mechanism may use induced changes in channel diameter, within the centrally tapered region of the transporter, to communicate the status of oppositely facing gates.

Conclusions

The NPC is comprised of a symmetrical or pseudo-symmetrical spoke–ring complex located in the plane of the nuclear envelope, that frames a central transport machine. In addition, data from other groups indicates that the NPC makes peripheral attachments to cytoplasmic filaments, particles, nucleoplasmic cages/baskets and the lamina to form an extended transport assembly (see Fig. 11; reviewed in references 7 and 55). Our 3D maps suggest that each half spoke is comprised of five domains that appear capable of moving relative to each other, providing an inherent conformational flexibility within the spoke–ring assembly. Therefore, it is hypothesized that the structural plasticity observed in vitro may play a role in the global regulation of transport in vivo, at the level of the NPC. In addition, the framework of the pore complex is firmly anchored within the nuclear envelope as the tip of each spoke penetrates into the nuclear lumen. In this way, a lumenal ring of nucleoporins is formed by the association of adjacent lumenal spoke domains with intervening radial arm dimers. Interestingly, the nuclear envelope appears to conform to the surface of the octagonal spoke complex while leaving the thin rings exposed to their respective cellular compartments (also see reference 33). However, the lumen between nuclear membranes may undergo osmotic swelling during the isolation of macro-nuclei. Hence, it is not known whether the membrane-associated NPC described in this work represents the in vivo conformation or merely a single structure in a range of possible structures (reference 34; and this work). Moreover, the visualization of the central transporter as an elongated centrally tapered cylinder, lends support to the proposed macromolecular lock hypothesis. In this model, it is suggested that substrate passage across the nuclear envelope may require two asynchronous gating events within the context of a central channel (4). High resolution data are now needed on distinct conformations of the spoke–ring complex and the associated transporter to extend our understanding of this unique transport machine.

This work has benefited from the suggestions of M. Rout and the support of N. Unwin. The computational biology was greatly aided by A. Leith who made available upgrades of SPIDER/WEB and D. Atkinson, who set up our computer network. We gratefully acknowledge the advice provided by R. Nolte on color slide and print making. Finally, we thank colleagues in the Department of Cell Biology, Stanford University School of Medicine and the Structural Studies Division, Medical Research Council Laboratory of

Molecular Biology, for access to and support of the Philips EM400 series microscopes.

This work was supported by the National Institutes of Health (R01 GM45377 and R01 GM29169).

Received for publication 22 September 1992 and in revised form 6 April 1993.

References

1. Adam, S. A., and L. Gerace. 1991. Cytosolic proteins that specifically bind nuclear location sequences are receptors for nuclear import. *Cell.* 66:837–847.
2. Aebi, U., J. Cohn, L. Buhle, and L. Gerace. 1986. The nuclear lamina is a meshwork of intermediate-type filaments. *Nature (Lond.).* 323: 560–564.
3. Akey, C. W. 1989. Interactions and structure of the Nuclear Pore Complex revealed by cryo-electron microscopy. *J. Cell Biol.* 109:955–970.
4. Akey, C. W. 1990. Visualization of transport-related configurations of the nuclear pore transporter. *Biophys. J.* 58:341–355.
5. Akey, C. W. 1991. Probing the structure and function of the nuclear pore complex. *Semin. Cell Biol.* 2:167–177.
6. Akey, C. W. 1992*a*. The Nuclear Pore Complex. *Curr. Opin. Struct. Biol.* 2:258–263.
7. Akey, C. W. 1992*b*. The nuclear pore complex: a macromolecular transporter. *In* Nuclear Trafficking. C. Feldherr, editor. Academic Press, New York. 31–70.
8. Akey, C. W., and D. S. Goldfarb. 1989. Protein import through the nuclear pore complex is a multi-step process. *J. Cell Biol.* 109:971–982.
9. Bataille, N., T. Helsen, and H. M. Fried. 1990. Cytoplasmic transport of ribosomal subunits microinjected into the *Xenopus* laevis oocyte nucleus: a generalized facilitated process. *J. Cell Biol.* 111:1571–1582.
10. Berrios, M., P. A. Fisher, and E. C. Matz. 1991. Localization of a myosin heavy chain-like polypeptide to Drosophila Nuclear Pore Complexes. *Proc. Natl. Acad. Sci.* 88:219–223.
11. Buhle, L., and U. Aebi. 1985. Correlation of surface topography of metal shadowed specimens with their negatively stained reconstructions. *Ultramicroscopy.* 16:436–450.
12. Carazo, M. J., and J. L. Carrascosa. 1987. Information recovery in missing angular data cases: an approach by the convex projections method in three-dimensions. *J. Microscopy.* 145:23–43.
13. Dabauvalle, M-C., B. Schulz, U. Scheer, and R. Peters. 1988. Inhibition of nuclear accumulation of karyophilic proteins in living cells by microinjection of the lectin wheat germ agglutinin. *Exp. Cell Res.* 174:291–296.
14. Dargemont, C., and L. C. Kuhn. 1992. Export of mRNA from microinjected nuclei of Xenopus laevis oocytes. *J. Cell Biol.* 118:1–9.
15. Dingwall, C., and R. A. Laskey. 1986. Protein import into the cell nucleus. *Ann. Rev. Cell Biol.* 2:367–390.
16. Dubochet, J., M. Adrian, J. Chang, J. C. Homo, J. Lepault, A. W. McDowall, and P. Shultz. 1988. Cryo-electron microscopy of vitrified specimens. *Q. Rev. Biophys.* 21:129–228.
17. Dworetzky, S. I., and C. M. Feldherr. 1988. Translocation of RNA-coated gold particles through the nuclear pores of oocytes. *J. Cell Biol.* 106:575–584.
18. Faberge, A. C. 1973. Direct demonstration of eightfold symmetry in nuclear pores. *Z. Zellforsch Mikrosk. Anat.* 136:183–190.
19. Featherstone, C., M. Darby, and L. Gerace. 1988. A monoclonal antibody against the nuclear pore complex inhibits nucleocytoplasmic transport of protein and RNA in vivo. *J. Cell Biol.* 107:1289–1297.
20. Feldherr, C. M. 1962. The nuclear annuli as pathways for nucleocytoplasmic exchanges. *J. Cell Biol.* 14:65–72.
21. Feldherr, C. M. 1992. Overview of signal-mediated transport. *In* Nuclear Trafficking, C. M. Feldherr, editor. Academic Press, New York. 15–28.
22. Feldherr, C. M., and D. Akin. 1990. The permeability of the nuclear envelope in dividing and nondividing cell cultures. *J. Cell Biol.* 111:1–8.
23. Feldherr, C. M., E. Kallenback, and N. Schultz. 1984. Movement of a karyophilic protein through the nuclear pores of oocytes. *J. Cell Biol.* 99:2216–2222.
24. Finlay, D. R., D. D. Newmeyer, T. M. Price, and D. J. Forbes. 1987. Inhibition of *in vitro* nuclear transport by a lectin that binds to nuclear pores. *J. Cell Biol.* 104:189–200.
25. Forbes, D. J. 1992. Structure and function of the nuclear pore. *Ann. Rev. Cell Biol.* 8: 495–527.
26. Frank, J., B. Shimkin, and H. Dowse. 1981*a*. SPIDER-a modular software system for electron image processing. *Ultramicroscopy.* 6:343–358.
27. Frank, J., A. Verschoor, and M. Boublik. 1981*b*. Computer averaging of electron micrographs of 40S ribosomal subunits. *Science (Wash. DC).* 214:1353–1355.
28. Franke, W. W., and U. Scheer. 1970. The ultrastructure of the nuclear envelope of amphibian oocytes, a reinvestigation I: the mature oocyte. *J. Ultrastruc. Res.* 30:288–316.
29. Gerace, L., and B. Burke. 1988. Functional organization of the nuclear envelope. *Ann. Rev. Cell Biol.* 4:335–374.
30. Goldfarb, D. S., J. Gariepy, G. Schoolnik, and R. D. Kornberg. 1986. Synthetic peptides as nuclear localization signals. *Nature (Lond.).* 326:641–644.
31. Greber, U. F., and L. Gerace. 1992. Nuclear protein import is inhibited by an antibody to a lumenal epitope of a nuclear pore complex glycoprotein. *J. Cell Biol.* 116:15–30.
32. Greber, U. F., A. Senior, and L. Gerace. 1990. A major glycoprotein of the nuclear pore complex is a membrane-spanning polypeptide with a large lumenal domain and a small cytoplasmic tail. *EMBO (Eur. Mol. Biol. Organ.) J.* 9:1495–1502.
33. Goldberg, M. W., and T. D. Allen. 1992. High Resolution scanning electron microscopy of the nuclear envelope: demonstration of a new, regular, fibrous lattice attached to the baskets of the nucleoplasmic face of the nuclear pores. *J. Cell Biol.* 119:1429–1440.
34. Hinshaw, J. E., B. O. Carragher, and R. A. Milligan. 1992. Architecture and design of the nuclear pore complex. *Cell.* 69:1133–1141.
35. Holmes, K. C., and W. Kabsch. 1991. Muscle proteins: actin. *Curr. Opin. Struct. Biol.* 1:270–280.
36. Jarnik, M., and U. Aebi. 1991. Toward a more complete 3-D structure of the nuclear pore complex. *J. Struct. Biol.* 107:291–308.
37. Kedersha, N. L., J. E. Heuser, D. C. Chugani, and L. H. Rome. 1991. Vaults III. Vault ribonucleoprotein particles open into flower-like structures with octagonal symmetry. *J. Cell Biol.* 112:225–235.
38. Maquat, L. E. 1991. Nuclear mRNA export. *Curr. Opin. Cell Biol.* 3:1004–1012.
39. Maul, G. 1977. The nuclear and cytoplasmic pore complex: structure, dynamics, distribution and evolution. *Int. Rev. Cytol. Suppl.* 6:75–186.
40. Mehlin, H., B. Daneholt, and U. Skoglund. 1992. Translocation of a specific premessenger ribonucleoprotein particle through the nuclear pore studied with electron microscope tomography. *Cell.* 69:605–613.
41. Michaud, N., and D. S. Goldfarb. 1992. Microinjected U snRNAs are imported to oocyte nuclei via the nuclear pore complex by three distinguishable targeting pathways. *J. Cell Biol.* 116:851–861.
42. Milligan, R. A. 1986. A structural model for the nuclear pore complex. *In* Nucleocytoplasmic Transport. R. Peters and M. Trendelenburg, editors. Springer-Verlag New York Inc., New York. 111–122.
43. Moll, T., G. Tebb, U. Surana, H. Robitsch, and K. Nasmyth. 1991. The role of phosphorylation and the CDC28 protein kinase in cell cycle-regulated nuclear import of the *S. Cerevisiae* transcription factor SWI5. *Cell.* 66:743–758.
44. Moore, M. S., and G. Blobel. 1992. The two steps of nuclear import, targeting to the nuclear envelope and translocation through the nuclear pore, require different cytosolic factors. *Cell.* 69:939–950.
45. Newmeyer, D. D., and D. J. Forbes. 1990. An N-ethylmaleimide sensitive cytosolic factor necessary for nuclear protein import: requirement in signal-mediated binding to the nuclear pore. *J. Cell Biol.* 110:547–557.
46. Newmeyer, D. D., J. M. Lucocq, T. R. Burglin, and E. M. DeRobertis. 1986. Assembly in vitro of nuclei active in nuclear protein transport: ATP is required for nucleoplasmic accumulation. *EMBO (Eur. Mol. Biol. Organ.) J.* 5:501–510.
47. Newmeyer, D. D., and D. J. Forbes. 1988. Nuclear import can be separated into distinct steps in vitro: nuclear pore binding and translocation. *Cell.* 52: 641–653.
48. Nigg, E. A., P. A. Baeuerle, and R. Luhrmann. 1991. Nuclear import-export: in search of signals and mechanisms. *Cell.* 66:15–22.
49. Paine, P. L., L. C. Moore, and S. B. Horowitz. 1975. Nuclear envelope permeability. *Nature (Lond.).* 254:109–114.
50. Radermacher, M. 1988. Three dimensional reconstruction of single particles from random conical tilt series. *J. Electron Microsc. Tech.* 9:359–394.
51. Radermacher, M. 1992. The structure of the 50S ribosomal subunit from *E. coli* in frozen hydrated preparation reconstructed with SECReT. *Proc. Xth Eur. Congr. Electron Microsc.* In press.
52. Reichelt, R., A. Holzenburg, E. L. Buhle Jr., M. Jarnik, A. Englel, and U. Aebi. 1990. Correlation between structure and mass distribution of the nuclear pore complex and of distinct pore complex components. *J. Cell Biol.* 110:883–894.
53. Richardson, W. D., A. D. Mills, S. M. Dilworth, R. A. Laskey, and C. Dingwall. 1988. Nuclear protein migration involves two steps: rapid binding at the nuclear envelope, followed by slower translocation through nuclear pores. *Cell.* 52:655–664.
54. Ris, H. 1990. Application of low voltage high resolution SEM in the study of complex intracellular structures. *Proc. XII Int. Congr. Electron Microscopy.* San Francisco Press, Inc., San Francisco. 18–19.
55. Ris, H. 1991. The three-dimensional structure of the Nuclear Pore Complex as seen by high voltage electron microscopy and high resolution low voltage scanning electron microscopy. *EMSA Bulletin.* 21:1. 54–56.
56. Robbins, R., S. Dilworth, R. A. Laskey, and C. Dingwall. 1991. Two interdependent basic domains in the nucleoplasmin nuclear targeting sequence: identification of a new and distinct class of nuclear targeting sequence. *Cell.* 64:615–623.
57. Scheer, U., M-C. Dabauvalle, H. Merkert, and R. Benevente. 1988. The nuclear envelope and the organization of the pore complexes. *In* Nucleocytoplasmic Transport. R. Peters, editor. Academic Press, London. 5–25.

58. Sterne-Marr, R., J. M. Blevitt, and L. Gerace. 1992. O-linked glycoproteins of the nuclear pore complex interact with a cytosolic factor required for nuclear protein import. *J. Cell Biol.* 116:271–280.
59. Stewart, M., and S. Whytock. 1988. The structure and interactions of components of nuclear envelopes from *Xenopus* oocyte germinal vesicles observed by heavy metal shadowing. *J. Cell Sci.* 90:409–423.
60. Stewart, P. L., R. M. Burnett, M. Cyrklaff, and S. D. Fuller. 1991. Image reconstruction reveals the complex molecular organization of adenovirus. *Cell.* 67:145–154.
61. Stevens, B. J., and H. Swift. 1966. RNA transport from nucleus to cytoplasm in Chironomus salivary glands. *J. Cell Biol.* 31:55–77.
62. Unwin, P. N. T., and R. A. Milligan. 1982. A large particle associated with the perimeter of the nuclear pore complex. *J. Cell Biol.* 93:63–75.
63. Wang, G., C. Porta, Z. Chen, T. S. Baker, and J. E. Johnson. 1992. Identification of a Fab footprint site on an icosahedral virus by cryoelectron microscopy and x-ray crystallography. *Nature (Lond.).* 355:275–278.
64. Wozniak, R. W., E. Bartnik, and G. Blobel. 1989. Primary structure analysis of an integral membrane glycoprotein of the nuclear pore. *J. Cell Biol.* 108:2083–2092.
65. Zasloff, M. 1983. t-RNA transport from the nucleus in a eukaryotic cell: a carrier mediated translocation process. *Proc. Natl. Acad. Sci.* 80:6436–6440.